Applied Thermal Engineering 289 (2026) 129808

Contents lists available at ScienceDirect

Applied Thermal Engineering

journal homepage: www.elsevier.com/locate/apthermeng

Research Paper

Dynamic melting with a flow of phase change material over an electrical element for fast latent heat thermal energy storage cooling☆

Mohamed Bouzidi [a], Zehba Raizah [b], Bhupendra Singh Chauhan [c], Ahmad Hajjar [d], T. Anwor [e], Mansour Mohamed [a], Hammadi Khmissi [f,*], Mehdi Ghalambaz [g,h,**]

[a] Department of Physics, College of Science, University of Ha'il, Ha'il, P.O. Box 2440, Saudi Arabia
[b] Department of Mathematics, Faculty of Science, King Khalid University, Abha, Saudi Arabia
[c] Department of Mechanical Engineering, GLA University, Mathura, UP, India
[d] Center for Environmental Intelligence and College of Engineering and Computer Science, VinUniversity, Hanoi, Viet Nam
[e] Faculty of Science, King Mongkut University, Thailand
[f] Department of Physics, College of Science, Northern Border University, Arar 73213, Saudi Arabia
[g] Department of Mathematical Sciences, Saveetha School of Engineering, SIMATS, Chennai, India
[h] Refrigeration and Air Conditioning Technical Engineering Department, College of Technical Engineering, The Islamic University, Najaf, Iraq

ARTICLE INFO

Keywords:
Molten liquid cycle
Melting heat transfer
Nichrome element
Phase change material

ABSTRACT

Latent Heat Thermal Energy Storage (LHTES) systems, using phase change materials (PCMs), are promising solutions for efficient thermal energy management, especially in renewable energy storage and waste heat recovery. However, the low thermal conductivity of PCMs limits their performance. This study investigates a novel LHTES design that enhances thermal performance by integrating metal foam and dynamic melting. The system utilizes the hot liquid PCM as a working fluid, circulating between the shell and tube, with metal foam filling the space between them. A Nichrome heating element creates a liquid film that accelerates the melting of PCM. The study focuses on the effects of fin size (20 %–70 % of the enclosure width), inlet pressure, and heating element power on the thermal and flow behaviors. The finite element method was employed to solve the governing equations, considering both natural convection and the temperature difference between the PCM and metal foam. Key results show that increasing fin size reduces melting rates by obstructing convective flow, with a 27 % slower melting rate at 70 % fin size compared to 20 %. Increasing inlet pressure from 500 Pa to 3000 Pa enhanced melting rates by 51 % and 200 %, respectively. Similarly, increasing the heating element power from 250 W to 500 W accelerated melting by 189 %. The findings highlight the significant role of metal foam in improving heat transfer efficiency and reducing melting time. This work offers new insights into optimizing LHTES systems by integrating dynamic melting with metal foam, providing a more efficient solution for thermal energy storage compared to previous approaches.

1. Introduction

Latent Heat Thermal Energy Storage (LHTES) systems, utilizing phase change materials (PCMs), represent a significant step forward in addressing the global challenge of energy management, particularly in light of the intermittency of renewable energy sources and the dissipation of waste heat into the environment [1]. These systems facilitate the storage and release of thermal energy by utilizing the phase change

Abbreviations: A, outlet PCM area; C_p, Specific Heat Capacity; Cv, Specific Heat of Metal Foam; d_{fp}, Pore Diameter of Metal Foam; k, Thermal Conductivity; k_{MF}, Thermal Conductivity of Metal Foam; LHTES, Latent Heat Thermal Energy Storage; MF, Metal Foam; MVF, Melt Volume Fraction; Nu, Nusselt Number; PCM, Phase Change Material; Pin, Inlet Pressure; Pr, Prandtl Number; Q_0, Heat Generation Rate; Q_{latent}, Latent Heat Transfer; $Q_{sensible}$, Sensible Heat Transfer; Re, Reynolds Number; V, Volume; V_{out}, Outlet Velocity; α, Thermal Diffusivity; β, Thermal Expansion Coefficient; κ, Permeability of Metal Foam; μ, Dynamic Viscosity; ρ, Density; φ, Phase field variable.

☆ This article is part of a Special issue entitled: 'Cold Storage & Cooling Systems' published in Applied Thermal Engineering.

* Corresponding author.
* Corresponding author at: Department of Mathematical Sciences, Saveetha School of Engineering, SIMATS, Chennai, India.
E-mail addresses: hammadi.ali@nbu.edu.sa (H. Khmissi), ghalambaz.mehdi@gmail.com (M. Ghalambaz).

https://doi.org/10.1016/j.applthermaleng.2026.129808
Received 15 September 2025; Received in revised form 23 November 2025; Accepted 12 January 2026
Available online 15 January 2026

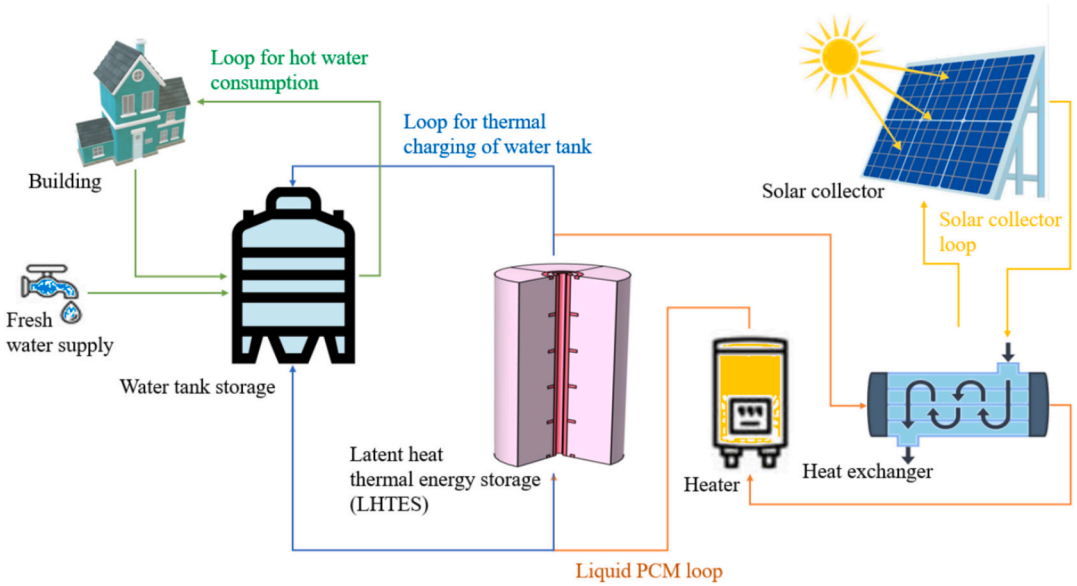

Fig. 1. Schematic representation of a high-intensity solar thermal configuration for space heating in buildings, illustrating the integration of a solar energy absorber, an LHTES module, and a thermal storage tank for enhanced energy management.

behavior of PCMs, offering a dispatchable solution with superior heat storage capacity, a diverse range of PCM options, and nearly isothermal operation, requiring only a single hermetic container without additional infrastructure like salt pumps or heating traces [2]. Such attributes make LHTES highly practical for applications such as solar thermal energy storage, thermal regulation in buildings [3], and various industrial processes [4]. However, the effectiveness of these systems has been limited by the low thermal conductivity of PCMs, which restricts the rate of heat exchange between PCMs and heat sources or sinks, resulting in slow phase transition times and reducing their overall efficiency [2,4,5]. The present study addresses this challenge by exploring innovative techniques to enhance the heat transfer properties of LHTES systems, with a focus on metal foams and dynamic melting.

To overcome the thermal conductivity barrier, a variety of innovative enhancement techniques have been explored, each contributing unique improvements to LHTES efficiency [6]. Hybrid techniques, combining multiple strategies, have shown promise in enhancing PCM performance, while Nano-enhanced PCM can increase thermal conductivity by up to 32 %, albeit with a corresponding reduction in latent heat by the same percentage [1,4]. Shape-stabilized PCMs offer a remarkable enhancement, boosting heat transfer rates by 3 to 10 times, making them ideal for solar collectors and photovoltaic-based recovery systems [4]. Magnetic fields improve melting and solidification performance by adjusting parameters like magnetic number and Hartmann number, influenced by container geometry and orientation [7]. Magnetic fields, ultrasonic vibration, and electrohydrodynamics further enhance heat transfer by manipulating fluid flow and heat conduction, contrasting with conventional methods like fins, which may compromise capacity [8]. Meanwhile, cavity geometry designs (e.g., spheres, squares) affect thermal efficiency, with nanoparticles in fluids accelerating cooling processes [2].

While these advancements have contributed to the optimization of PCM-based systems, a gap remains in the integration of dynamic melting techniques with metal foams to improve heat transfer. The present study aims to fill this gap by investigating the effects of dynamic melting, metal foam integration, and fin configurations on LHTES performance. These advancements, supported by materials like MXene with a 16 % conductivity increase and 94 % efficiency, underscore the transformative potential of LHTES, driving sustainable energy solutions across diverse sectors [4].

PCMs represent a pivotal technology in LHTES, leveraging their ability to absorb and discharge significant quantities of energy during phase transitions, a property that renders them particularly effective for applications demanding efficient thermal regulation, such as solar energy systems and domestic heating. For instance, an experimental study on convection-induced melting of lauric acid within a rectangular cavity revealed that the inclination angle plays a decisive role in shaping natural convection flows, which in turn govern the heat transfer rate and overall melting duration [9]. These findings emphasize the importance of optimizing natural convection flows through proper enclosure design. Within the hot wall temperature interval of 55–70 °C, the horizontal configuration enclosure was found to be over twice as large as a vertical one, underscoring the role of enclosure orientation in optimizing PCM performance. Similarly, a novel scraped surface heat exchanger designed for solar LHTES showed that scraping solidified PCM from heat transfer surfaces increased the heat release rate by two to three times compared to non-scraping modes, fully extracting 11.9 MJ of latent energy in a shorter duration [10]. These studies emphasize the crucial importance of enhancing heat transfer mechanisms and optimizing system design to maximize the efficacy of PCM-based systems.

Further advancing the understanding of PCM applications, numerical studies provide insights into optimizing thermal energy storage systems under complex conditions. A numerical investigation of non-Newtonian PCM flow in finned rectangular enclosures revealed that increasing the number of solid fins from one to three substantially reduced charging time, despite the material's inherently poor thermal conductivity [11]. This enhancement is primarily ascribed to the increased effective heat transfer area generated by the incorporation of fins, demonstrating a practical approach to overcoming PCM limitations. These studies emphasize that while PCMs offer significant energy storage potential, their effectiveness is contingent upon innovative design strategies, such as enclosure orientation, surface scraping, and fin integration, to address challenges like low thermal conductivity and slow phase transition rates [9–11]. While these findings highlight essential strategies, additional research is needed to fully understand the long-term effects of different PCM configurations on thermal performance.

Metal foams and porous media have emerged as transformative tools for enhancing heat transfer in enclosures across various engineering applications, including thermal management in electronics, photovoltaic systems, and industrial heat exchangers. These materials improve convective and conductive heat transfer by increasing surface area and

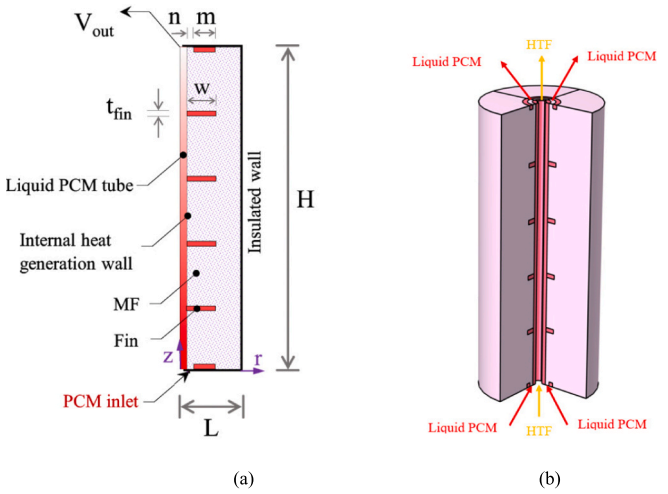

Fig. 2. The structural layout of the shell-and-tube thermal storage system incorporating a metal foam section and fins, (a) The employed coordinate framework along with the physical domains; (b) A schematic 3D representation of the axis-symmetric model.

Table 1
The width of fin across different designs.

Cases	W	P_{in} (Pa)	Q_0 (W)	PCM's V_{out} (m/s)
C_1	0.2 L	3000	500	0.22826
C_2	0.25 L	3000	500	0.22577
C_3	0.3 L	3000	500	0.22402
C_4	0.35 L	3000	500	0.22262
C_5	0.40 L	3000	500	0.22123
C_6	0.45 L	3000	500	0.21969
C_7	0.50 L	3000	500	0.21796
C_8	0.55 L	3000	500	0.21593
C_9	0.60 L	3000	500	0.21356
C_{10}	0.65 L	3000	500	0.21072
C_{11}	0.70 L	3000	500	0.20727
C_{12}	0.25 L	500	500	0.04782
C_{13}	0.25 L	1000	500	0.08825
C_{14}	0.25 L	1500	500	0.12572
C_{15}	0.25 L	2000	500	0.16087
C_{16}	0.25 L	2500	500	0.19412
C_{17}	0.70 L	3000	250	0.20727
C_{18}	0.70 L	3000	500	0.20727
C_{19}	0.70 L	3000	750	0.20727
C_{20}	0.70 L	3000	1000	0.20727
C_{21}	0.70 L	3000	1250	0.20727
C_{22}	0.70 L	3000	1500	0.20727

altering flow dynamics within enclosures. For example, recent research demonstrates that incorporating metal foams in photovoltaic thermal systems boosted thermal efficiency by 32 %, and in non-Newtonian fluid systems, heat transfer increased by 44 % with the introduction of porous media [12,13].

The application of metal foams in LHTES has garnered significant interest, particularly due to their ability to increase heat transfer rates and reduce melting times in PCM-based systems. Research has demonstrated that metal foams significantly improve heat transfer efficiency and shorten melting durations in PCM-based configurations. For instance, a numerical investigation on PCM integrated with metal foam featuring Kelvin cell structures demonstrated that raising the cell per length (CPL) improves the melting progression, reducing the overall time required for complete phase transition and facilitating faster energy accumulation, particularly in smaller enclosures [14]. These findings highlight the role of metal foams in overcoming the limitations of low-conductivity PCMs and improving energy storage performance.

The primary objective of the present work is to explore the use of dynamic melting and metal foam integration to enhance the performance of LHTES systems. By employing dynamic melting, which utilizes the forced convection of superheated liquid PCMs, we aim to accelerate the phase change process and improve overall system efficiency. The study specifically investigates the effects of varying fin sizes, inlet pressures, and heating rates on the melting process, providing new insights into optimizing LHTES performance. The dynamic melting offers applications for portable and fast charging of LHTES units.

2. Model description and governing equations

2.1. Model description

LHTES technologies are essential to the advancement of solar energy systems, as they address the inherent intermittency of solar power, which is influenced by both atmospheric conditions and diurnal cycles. LHTES systems are capable of storing significant amounts of thermal energy at the phase change (fusion) temperature of the storage medium, allowing for high energy density within a compact volume. This enables adequate compensation for fluctuations in solar energy availability.

Fig. 1 displays a diagrammatic view of a focused sunlight heating setup intended for indoor warming purposes. The system is composed of a solar collector, a thermal storage tank, an LHTES unit, and the corresponding circulation pumps. In operation, the concentrated solar collector heats water, which is then circulated through a heat exchanger via a pump. Simultaneously, a molten PCM is circulated through the LHTES unit and the same heat exchanger. Before re-entering the LHTES, the liquid PCM passes through an auxiliary electric heater that ensures the PCM reaches the desired temperature, thereby facilitating effective charging of the LHTES unit.

Discharging of the LHTES occurs through the flow of water within the inner tube of the storage unit, establishing a circulation loop between the LHTES and the domestic hot water reservoir. The storage reservoir subsequently supplies heated water to the building as required. During periods of low energy demand or excess solar energy generation, the LHTES is charged using the surplus thermal energy. Conversely, when demand increases, the hot water tank can draw thermal energy from the LHTES unit, ensuring a continuous and responsive supply of thermal energy for building heating needs.

Fig. 2 illustrates the shell-and-tube configuration adopted for designing the LHTES system in this study. The liquid PCM enters the shell region under a gauge pressure P_{in} and exits through the top outlet at atmospheric pressure (zero relative pressure). The HTF flows in the inner tube. Gravity acts from top to bottom, so it is opposite to the flow direction. The tube structure and fins are composed of nichrome, a material commonly used in electrical heating elements. The tube wall has a thickness of t_{tube} and internal radius $R = 6.35$ mm. The shell height is 0.4 m, and the shell radius is $13R$. The shell width (L), including the embedded element, is calculated by subtracting the tube radius (R) from the shell radius ($13R$), resulting in: $L = 13R - R = 12R$. There are fins with a thinness of 6 mm, and fin length of W. The space inside the shell is filled with copper metal foam and PCM. There is a port at the bottom of the enclosure where the heated liquid PCM enters, with an inlet temperature of T_{in} and an inlet pressure of P_{in}. There is also an exit port at the top where the liquid PCM can leave the enclosure. The flow of hot PCM initiates the transfer of thermal energy to the surrounding PCM in the domain. For an enclosure at subcooled status, there is no way for the molten PCM to enter the enclosure, nor is there a path between the PCM inlet and outlet. To create an initial path between the inlet and outlet ports, the nichrome tube and fins are subjected to an electrical current, generating heat at a rate of Q_0. This generated heat melts the PCM next to the nichrome tube, which in turn melts the nearby PCM and creates a layer of liquid PCM between the inlet and outlet ports. This allows an initial flow of molten PCM within the enclosure. As the flow continues, the liquid PCM layer expands, and the electrical heater will no longer be needed to generate heat. Thus, the heat generation in the nichrome domain is controlled by the flow rate at the output port as:

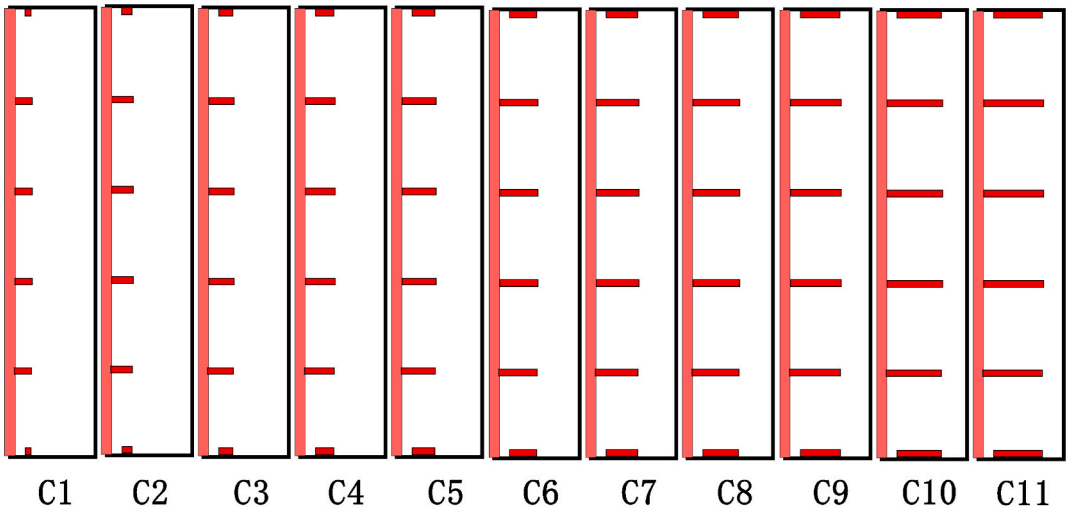

Fig. 3. Different fin sizes in the energy storage unit.

$$Q = Q_0 \times \begin{cases} 1 & \dfrac{V_{Out}(t)}{V_{Out}} < \dfrac{1}{3} \\ 0 & \dfrac{V_{Out}(t)}{V_{Out}} \geq \dfrac{1}{3} \end{cases} \tag{1}$$

where V_{Out} is the velocity of outlet liquid PCM when the PCM is fully melted, and there is a steady state flow of molten PCM through the enclosure. Solving the steady-state equations for the enclosure when all PCM is in the molten state yields: where A is the outlet PCM area, dA is an element of the outlet surface, and uz is the velocity component of the liquid PCM in the z-direction. Indeed, V_{Out} represents the maximum possible average velocity of PCM exiting through the outlet port. During the simulations, the average PCM outlet velocity as a function of time is computed as $V_{Out}(t) = A^{-1}\int_A u_z(t)dA$. Here, $V_{\mathrm{Out}}(t)$ computes the average velocity of the outlet PCM during the melting process. As long as the outlet velocity is fairly small ($V_{\mathrm{Out}}(t)/V_{\mathrm{Out}} < 1/3$), the heating element remains on with a power of Q_0. The element then turns off when the liquid PCM film forms and the outlet velocity reaches $1/3 \times V_{\mathrm{Out}}$ or higher. The values of V_{Out} have been computed and reported in Table 1. Fig. 3 shows a schematic view of the model for various fin lengths (Cases C_1–C_{11}).

In the present configuration, the radial fins are an integral part of the nichrome heating element, providing both mechanical rigidity and an extended conduction path from the electrical element into the surrounding MF-PCM composite. Therefore, the goal of this work is not to compare 'finned versus fin-less' tubes, which have been extensively studied in previous LHTES configurations, but rather to quantify how fin length influences dynamic melting when fins, metal foam, and forced PCM recirculation are simultaneously present.

2.2. Governing equations

The physical model consists of two separate regions: the nichrome tube structure and the MF-PCM domain, which are interconnected. The heat conduction process within these regions is described using the governing equation formulated in cylindrical coordinates in the internal heat generation nichrome wall and can be articulated as:

$$(\rho C_p)_{Nichrome}\frac{\partial T}{\partial t} = k_{Nichrome}\left(\frac{1}{r}\frac{\partial}{\partial r}\left(r\frac{\partial T}{\partial r}\right) + \frac{\partial^2 T}{\partial z^2}\right) + Q_{Nichrome} \tag{2}$$

In this context, k, ρ, and C_p denote the thermal conductivity, density, and specific heat capacity, respectively. The subscript "Nichrome" refers to the properties associated with the tube wall and fins. Q_{Nichrome} is the heat generation term with unit W/m^3. The magnitude of Q_{Nichrome} is adjusted with the volume of the Nichrome region to produce the heat rate of Q_0. Furthermore, t and T represent the time and temperature distribution, respectively. As depicted in Fig. 2, the cylindrical coordinate structure is established by the radial and vertical axes.

The open-cell structure of metal foam facilitates the penetration and distribution of molten PCM within its porous matrix. Thermal gradients formed within the liquid PCM generate buoyancy-driven forces, thereby inducing natural convective motion throughout the porous structure. Additionally, any externally imposed flow of the liquid PCM contributes to forced convection. The combined effect of these mechanisms results in mixed convection within the MF-PCM domain. Consequently, accurate thermal analysis in such systems necessitates the simultaneous solution of the governing equations for fluid flow and phase transition within the MF-PCM region. The melt fraction across the computational domain is tracked using the enthalpy–porosity approach to model the phase change [15]. To distinguish between the temperatures of the metal foam and the PCM, a local thermal non-equilibrium (LTNE) framework is adopted. Additionally, non-Darcy flow effects are incorporated into the analysis. Consequently, the governing differential equations describing the physical model are formulated as follows [16–18]:

$$\frac{\partial u_z}{\partial z} + \frac{1}{r}\frac{\partial (r u_r)}{\partial r} = 0 \tag{3}$$

z-momentum equation in PCM domain:

$$\frac{\rho_{\mathrm{PCM}}}{\varepsilon}\left(\frac{\partial u_z}{\partial t} + \frac{1}{\varepsilon}\left(u_z\frac{\partial u_z}{\partial z} + u_r\frac{\partial u_z}{\partial r}\right)\right) = -\frac{\partial p}{\partial z} + \frac{\mu_{\mathrm{PCM}}}{\varepsilon}\left(\frac{\partial^2 u_z}{\partial z^2} + \frac{1}{r}\frac{\partial}{\partial r}\left(r\frac{\partial u_z}{\partial z}\right)\right) + u_z\left(-\frac{\rho_{\mathrm{PCM}} C_F}{\sqrt{\kappa}}|u| + \frac{A_{mush}(1-\varphi(T))^2}{\lambda_{mush}+\varphi^3(T)} - \frac{\mu_{\mathrm{PCM}}}{\kappa}\right) + g(\rho\beta)_{\mathrm{PCM}}(T - T_0) \tag{4}$$

r-momentum equation in PCM domain:

$$\frac{\rho_{\mathrm{PCM}}}{\varepsilon}\left(\frac{\partial u_r}{\partial t} + \frac{1}{\varepsilon}\left(u_z\frac{\partial u_r}{\partial z} + u_r\frac{\partial u_r}{\partial r}\right)\right) = -\frac{\partial p}{\partial r} + \frac{\mu_{\mathrm{PCM}}}{\varepsilon}\left(\frac{1}{r}\frac{\partial}{\partial r}\left(r\frac{\partial u_r}{\partial r}\right) - \frac{u_r}{r^2} + \frac{\partial^2 u_r}{\partial z^2}\right) + u_r\left(-\frac{\rho_{\mathrm{PCM}} C_F}{\sqrt{\kappa}}|u| - \frac{\mu_{\mathrm{PCM}}}{\kappa} - \frac{A_{mush}(1-\varphi(T))^2}{\lambda_{mush}+\varphi^3(T)}\right) \tag{5}$$

Energy equation in PCM domain:

Table 2
Overview of the thermophysical properties of the materials involved in the system.

Materials	μ (kg/m.s)	β (1/K)	T_m (°C)	L (kJ/kg)	C_p (J/kg.K)	k (W/m.K)	ρ (kg/m^3)
Paraffin (solid/liquid) [25–27]	0.0036	0.00091	49–54	176	2700/2900	0.21/0.12	916/790
Nichrome [28]	–	–	–	–	450	11.3	8400
Water [29]	0.000957	0.00021	–	–	4179	0.613	997.1

$$(\rho C_p)_{PCM}\left(\varepsilon\frac{\partial T_{PCM}}{\partial t}+\left(u_z\frac{\partial T_{PCM}}{\partial z}+u_r\frac{\partial T_{PCM}}{\partial r}\right)\right)=$$
$$\frac{\partial}{\partial z}\left(k_{eff,PCM}\frac{\partial T_{PCM}}{\partial z}\right)+\frac{1}{r}\frac{\partial}{\partial r}\left(k_{eff,PCM}r\frac{\partial T_{PCM}}{\partial r}\right)-\varepsilon(\rho L)_{PCM}\frac{\partial\varphi(T)}{\partial t}+h_v(T_{MF}-T_{PCM}) \quad (6)$$

Energy equation in MF domain:

$$(\rho C_p)_{MF}(1-\varepsilon)\frac{\partial T_{MF}}{\partial t}=\frac{\partial}{\partial z}\left(k_{eff,MF}\frac{\partial T_{MF}}{\partial z}\right)+\frac{1}{r}\frac{\partial}{\partial r}\left(k_{eff,MF}r\frac{\partial T_{MF}}{\partial r}\right)-h_v(T_{MF}-T_{PCM}) \quad (7)$$

where r coming from the radial coordinate system, u_r is the radial velocity, and $|u|=\sqrt{(u_r^2+u_z^2)}$ is the velocity magnitude. The symbols μ, g, β, and L, indicates the dynamic viscosity, gravity magnitude, volumetric thermal expansion coefficients, and latent heat of fusion, respectively. The subscripts of PCM, MF, eff denotes the PCM material, metal foam material, and effective properties, respectively.

In this formulation, κ and C_F denote the porous medium's permeability and the Forchheimer coefficient, respectively. The volumetric heat transfer coefficient, h_v, which will be elaborated upon in a subsequent section, represents the heat exchange between the pore-filling PCM and the surrounding porous structure. To ensure negligible velocity components within the solid PCM regions, two parameters A_{mush} and λ_{mush} are introduced, assigned high and low values, respectively ($A_{mush}=10^{10}$ Pa.s/m^2 and $\lambda_{mush}=0.001$). Additionally, a simplified artificial dynamic viscosity formulation is employed to improve numerical convergence, defined as $\mu_{PCM}=(1\text{-}\varphi)\times\mu_{art}+\varphi\times\mu_{PCM,l}$, in which μ_{art} denotes the artificial viscosity and is assigned a value of 10^4 Pa.s [19].

The effective thermal conductivities of both the metal foam and the PCM are incorporated, acknowledging that the pore structure significantly influences these values [20]. The melting volume fraction, φ, is governed by the PCM temperature, as described below [21,22]:

$$\varphi(T)=\begin{cases}0 & T<T_f-\frac{\Delta T_f}{2}\ (\text{Solidous phase})\\ \frac{(T-T_f)}{\Delta T_f}+\frac{1}{2} & T_f-\frac{\Delta T_f}{2}\le T\le T_f+\frac{\Delta T_f}{2}\ (\text{Solidous-Liquid region})\\ 1 & T>T_f+\frac{\Delta T_f}{2}\ (\text{Liquid phase})\end{cases} \quad (8)$$

In this context, ΔT_f represents the temperature interval over which the phase transition takes place around the fusion point T_f. The governing formulations incorporate the porosity (ε) and the average permeability (κ) of the porous medium. The permeability (κ) [23] and the effective thermal conductivity (k) of the metal foam are evaluated using the following expressions [16,20]:

$$k=\frac{k_{MF}(1-\varepsilon)}{3} \quad (9)$$

$$\kappa=\frac{1}{\kappa_{tor}(\kappa_{tor}-1)}\left(\frac{\varepsilon d_{fp}\sqrt{\frac{\kappa_{tor}}{3\varepsilon}}}{6}\right)^2 \quad (10)$$

In these equations, k_{MF} denotes the bulk thermal conductivity of the metal foam, while d_{fp} and κ_{tor} are defined as follows [23]:

$$\frac{d_{fs}}{d_{fp}}=\frac{59}{50}\left(\frac{1-\varepsilon}{3\pi}\right)^{\frac{1}{2}}\left(1-\exp\left(\frac{\varepsilon-1}{0.04}\right)\right)^{-1} \quad (11)$$

$$\frac{1}{\kappa_{tor}}=\frac{1}{\varepsilon}\left[\frac{3}{4}+\frac{(9-8\varepsilon)^{\frac{1}{2}}}{2}\cos\left\{\frac{4}{3}\pi+\frac{1}{3}\cos^{-1}\left(\frac{8\varepsilon^2+27-36\varepsilon}{(9-8\varepsilon)^{\frac{3}{2}}}\right)\right\}\right] \quad (12)$$

In this context, d_{fp} is calculated based on the pores-per-inch (PPI) specification of the metal foam [23]:

$$d_{fp}=0.0254/PPI \quad (13)$$

Here for the metal foam, PPI = 40 was considered. The Frochheimer coefficient is determined using the specified analytical eq. [23]:

$$C_F=\left(\frac{1}{1-\varepsilon}\right)^{0.132}\left(\frac{d_{fs}}{d_{fp}}\right)^{-1.63}\times 0.00212 \quad (14)$$

The study presented in [24] defines h_v as a performance of the Nusselt number:

$$h_v=\left(\frac{1}{d_{fs}}\right)^2 k_{PCM}Nu_v \quad (15)$$

where Nu_v is subsequently determined for small pore-scale Reynolds numbers using the following relations [24]:

$$Nu_v=\begin{cases}76.99-152.01\times\varepsilon+75.04\times\varepsilon^2 & 0\le Re\le 0.1\\ (1.72+1.71\times\varepsilon-3.46\times\varepsilon^2)\times Re^{0.26}\times Pr^{0.28} & 0.1<Re\le 1\end{cases} \quad (16)$$

Here, $Pr=\rho_{PCM}\times\mu_{PCM}/\alpha_{PCM}$ where $\alpha_{PCM}=k_{PCM}/(\rho C_p)_{PCM}$. The pore scale Reynolds number (Re) is evaluated using the relation $Re=d_{fs}\times u_{PCM}\times\rho_{PCM}/\mu_{PCM}$. This formulation aligns well with the low or negligible velocity magnitudes observed for PCM distributed within the metal foam structure [19].

In conclusion, the effective thermal conductivity of the PCM, $k_{eff,PCM}$, is estimated based on the approaches detailed in [16,20]. A linear weighting method is applied to compute the thermophysical properties across the phase change interface:

$$k_{eff,PCM}=k_{PCM}\left(\frac{\varepsilon+2}{3}\right) \quad (17)$$

$$(\rho C_p)_{PCM}=\varphi(\rho C_p)_s+(1-\varphi)(\rho C_p)_l \quad (18)$$

$$\rho_{PCM}=\varphi\rho_s+(1-\varphi)\rho_l \quad (19)$$

In this formulation, subscripts s and l are used to denote the solid and liquid phases of the PCM, respectively. The thermophysical properties of paraffin, metal foam, and the structural components (tube and fins) are summarized in Table 2.

2.3. Initial and boundary conditions

Continuity conditions for both temperature and heat flux were imposed at the interfaces of connected walls. In the case of LTNE, temperature continuity was maintained, whereas the heat flux continuity was partitioned between the PCM phases and porous matrix as follows [19]:

$$q_{nichrome}=(1-\varepsilon)q_{MF}+\varepsilon q_{PCM} \quad (20)$$

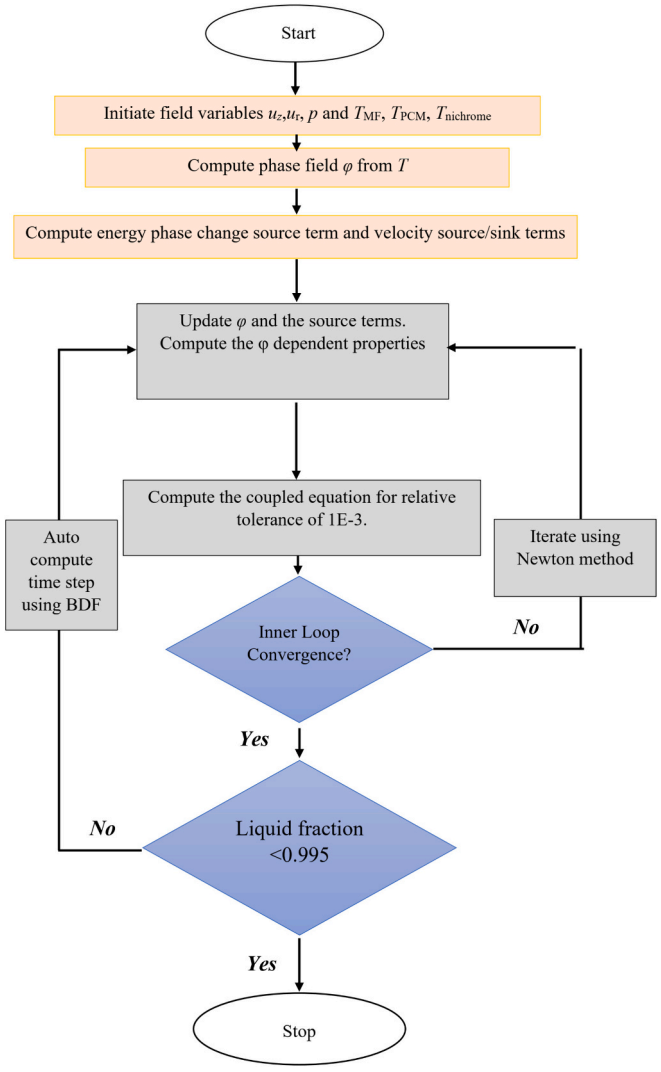

Fig. 4. Flowchart of the numerical procedure employed for solving the governing equations.

Table 3
Mesh configuration details corresponding to varying values of the mesh control parameter N_m.

N_m	Tube wall and fins elements	MF-PCM elements	Total elements
3	327	3283	3622
4	578	5946	6502
5	1291	9359	10,358
6	1652	12,894	13,876
7	2419	17,386	19,409

A consistent inlet temperature of $T_h = T_f + 15\ ^\circ C$ was employed at the inlet liquid PCM port. A gauge pressure P_{in} was applied at the liquid PCM inlet. The LHTES unit was assumed to initially operate at a supercooled temperature of $T_c = T_f$-15 °C, where $T_f = 51.5\ ^\circ C$. Except for the inlet and outlet, which were treated independently, all other surfaces were assigned no-slip and impermeability boundary conditions. Thermal insulation was assumed along the tube's inner surface and the shell's outer surface. The outlet was subjected to an outflow condition characterized by zero relative pressure and a heat flux condition of -n.$q = 0$, where n represents the unit normal vector to the surface.

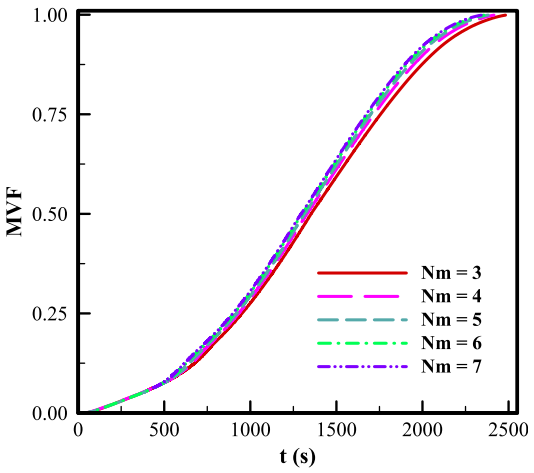

Fig. 5. Influence of mesh resolution on the MVF during the phase change for case C2 when $w = 0.25$ L at $P_{in} = 3000$ Pa, $Q_0 = 500$ W, and $V_{out} = 0.2$ m/s.

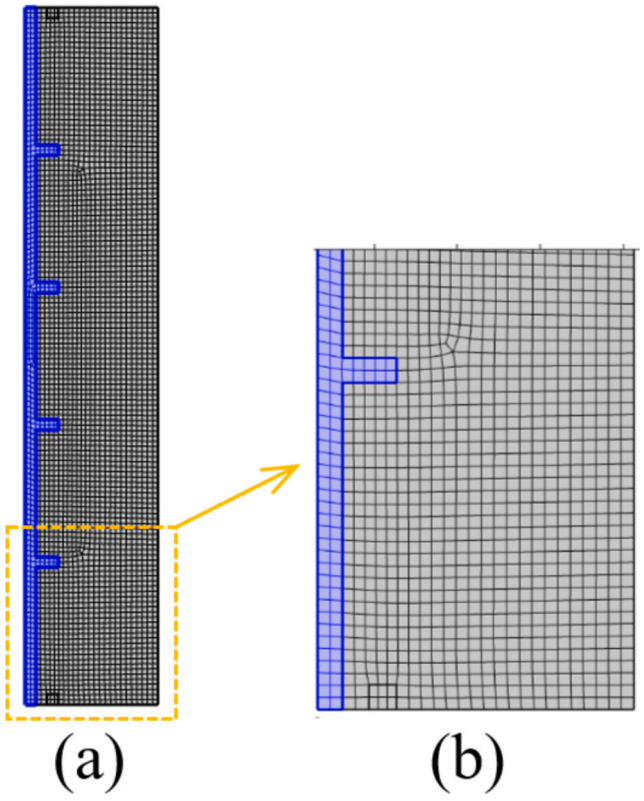

Fig. 6. (a): A broad depiction of the chosen grid layout ($Nm = 6$); (b): an in-depth portrayal of the lower portion.

2.4. Key parameters

Given the axisymmetric nature of the model, the integration is performed over the entire volume. The accumulated thermal energy is computed as the sum of both sensible and latent heat contributions:

$$Power = \frac{Q_{store}}{time} = \frac{Q_{latent} + Q_{sensible}}{time} \tag{21}$$

$$Q_{latent} = \varepsilon \oint_V (L\rho)_{PCM} \varphi dV \tag{22}$$

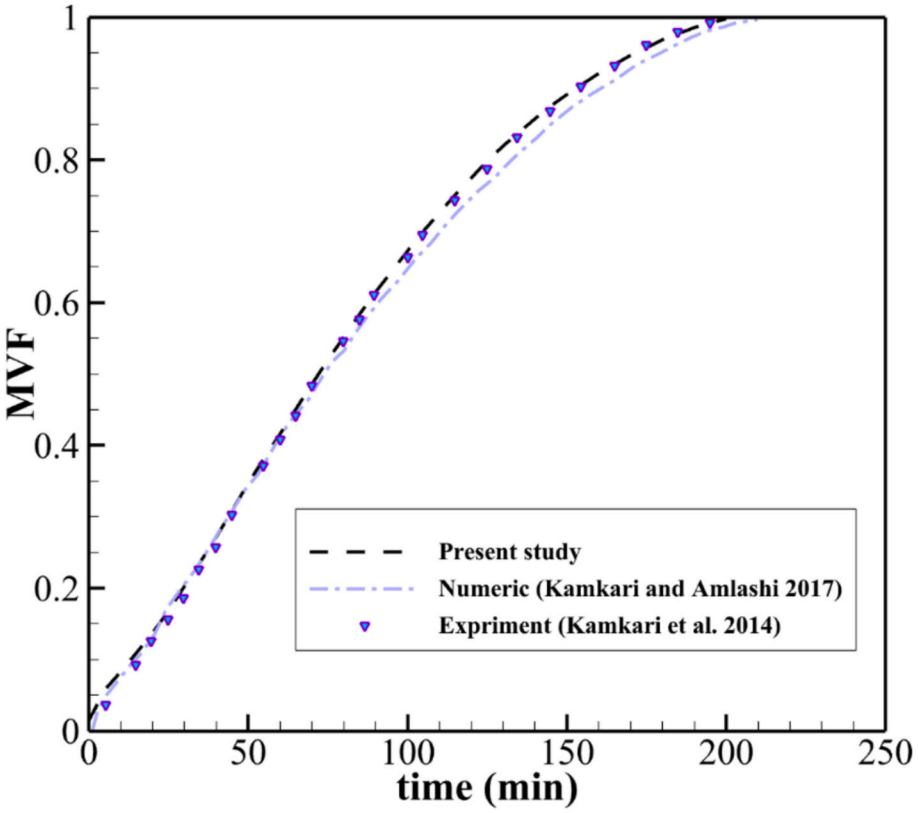

Fig. 7. Comparison of MVF evolution over time between the present study and the numerical results of Kamkari and Amlashi [37], as well as the experimental observations of Kamkari et al. [9].

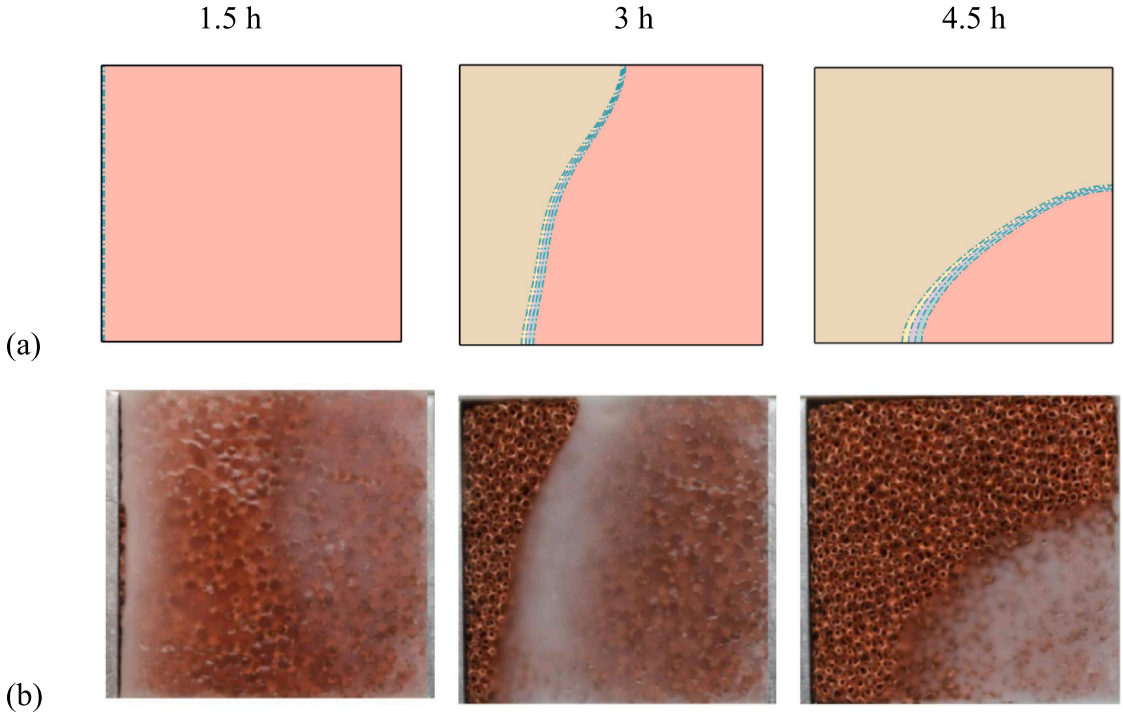

Fig. 8. Melting behavior of a paraffin wax–metal foam composite in the enclosure: (a) simulation results of the present study, and (b) corresponding empirical observations from [28].

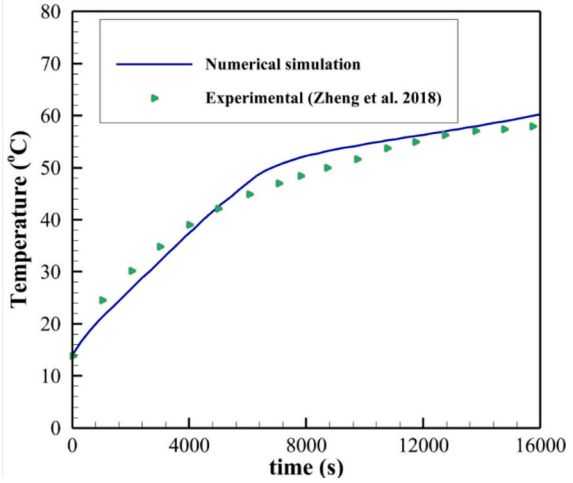

Fig. 9. Comparison of the wall average temperature for the enclosure heated from side and filled by coper metal foam experimented in [28] and the present simulation results.

$$Q_{sensible} = (\rho C_P)_{\mathrm{MF}} \oint_V (1-\varepsilon)(T_{\mathrm{MF}} - T_0)dV + \oint_V \left(\int_{T_0}^{T_{\mathrm{PCM}}} \varepsilon (\rho C_P)_{\mathrm{PCM}} dT \right) dV + (\rho C_P)_{\mathrm{nichrome}} \oint_V (T_{\mathrm{nichrome}} - T_0)dV \tag{23}$$

In this context, V denotes the volume occupied by a domain, and dV represents an infinitesimal volume element. MVF parameter, which represents the mean fraction of melted PCM, is determined as follows:

$$MVF = \frac{\oint_V (\varphi\varepsilon)dV}{\oint_V (\varepsilon)dV} \tag{24}$$

3. Computational techniques and simulation assessment

This section presents the computational methodology, grid independence assessment as well as validation of the computational model.

3.1. Finite element method

The governing mathematical relations, together with their corresponding boundary and initial constraints, were tackled by employing the finite element method (FEM) to accurately capture the phase change

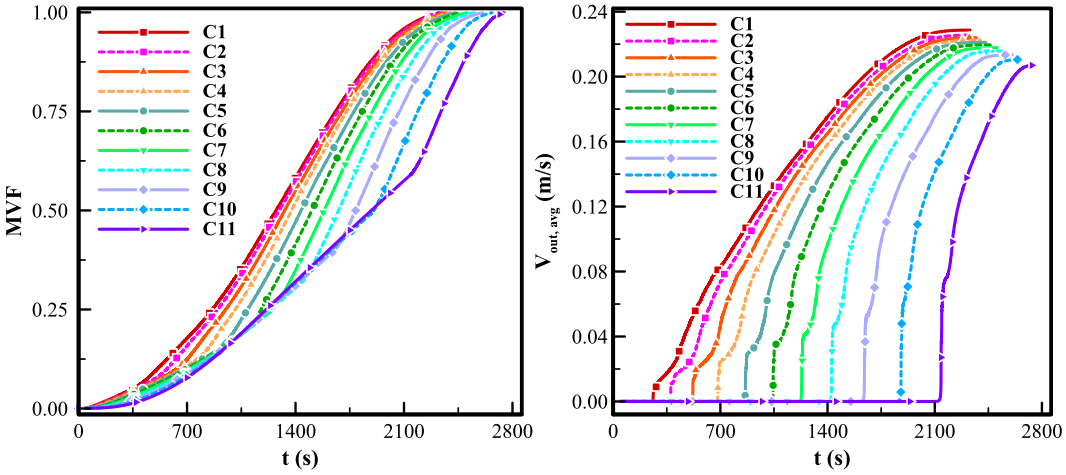

Fig. 10. MVF and the average PCM velocity at the outlet port over the melting process across different configurations at $P_{\mathrm{in}} = 3000$ Pa and $Q_0 = 500$ W.

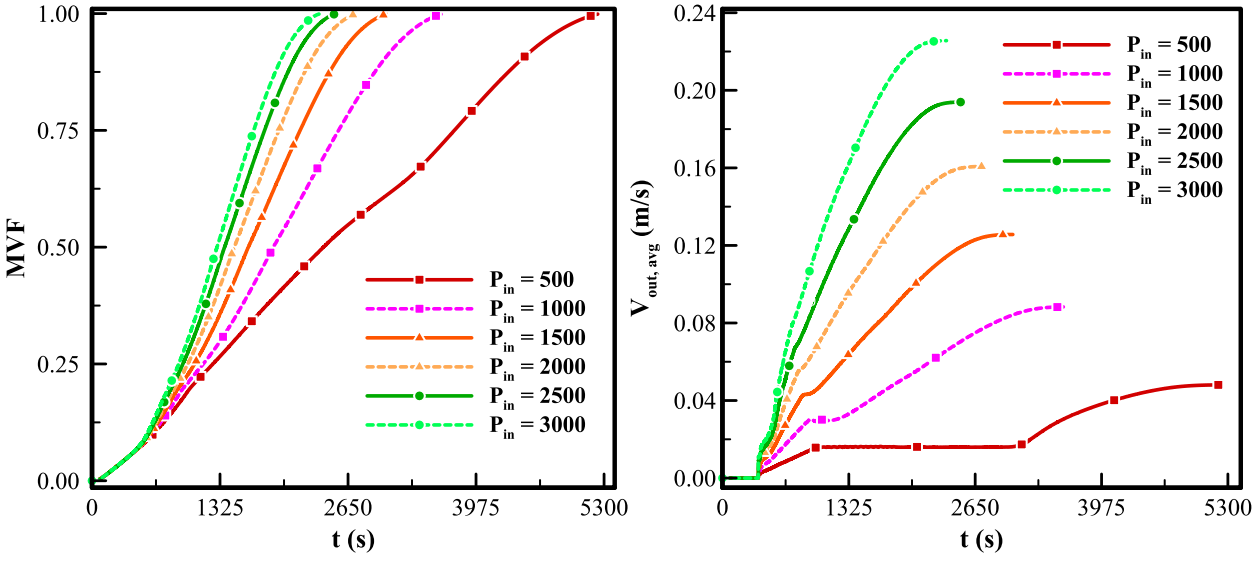

Fig. 11. MVF and the average PCM velocity at the outlet port during melting progression across various pressure measured in Pa at W = 0.25 L (C_2) and $Q_0 = 500$ W.

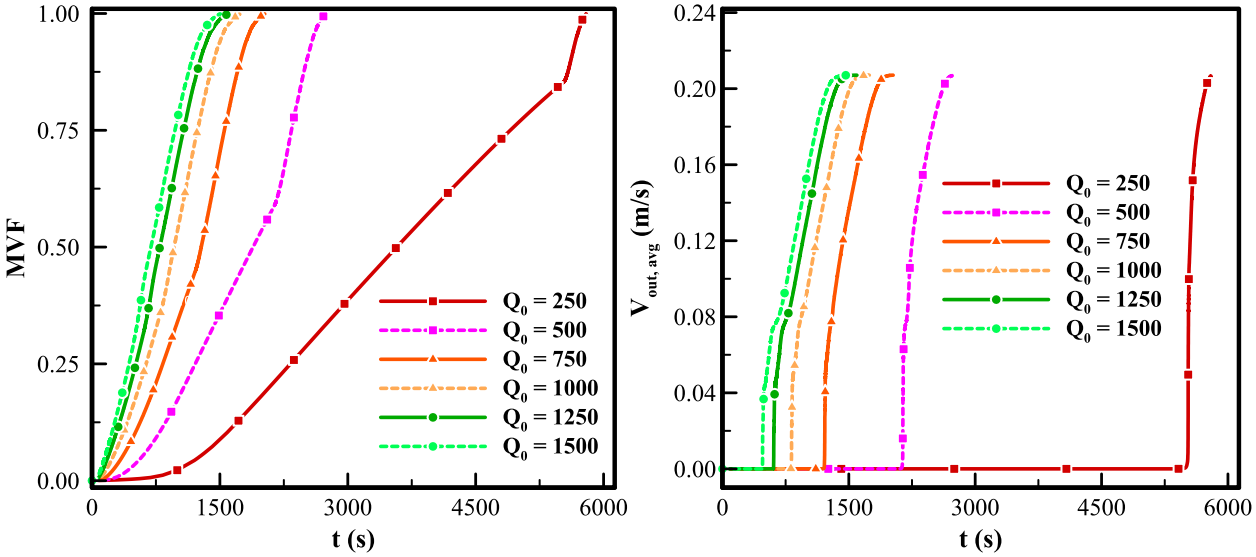

Fig. 12. MVF and the average PCM velocity at the outlet port during melting process for different Q_0 measure in W at w = 0.7 L (C_{11}), P_{in} = 3000 Pa and V_{out} = 0.207276 m/s.

effects [30,31]. The equations were first converted into their weak formulations, and a second-order discretization scheme was applied to both the thermal and momentum equations. Element-wise integration using Gauss quadrature yielded a set of algebraic residual relations, which were addressed through a coupled, iterative approach via the Newton–Raphson technique [32,33], incorporating a damping coefficient of 0.8 was employed to improve numerical stability and convergence. Parallel computations were carried out using the PARDISO solver in conjunction with the Newton scheme, allowing efficient use of multiple CPU cores [34,35]. Time stepping and convergence control were managed automatically using the first- and second-order backward differentiation formula (BDF), ensuring that the relative error remained below 1E-3 [36].

The FEM facilitated the generation of continuous and smooth solutions across the computational domain, offering the precision required for this study. Specified initial conditions were employed, after which the system was analyzed for phase transition and thermal storage behavior. At the start of each computational run, relevant thermophysical properties, such as the metal foam's effective thermal conductivity and permeability in the x and y directions were computed. The phase field variable (φ) was subsequently updated based on the PCM temperature distribution, and these properties were incorporated into the governing equations. The heat transfer and continuity equations were treated as fully coupled and solved iteratively. The simulation was programmed to terminate upon complete melting of the PCM, defined by a MVF equal to or exceeding 0.995, which served as the stopping criterion. Fig. 4 presents a schematic representation of the implemented computational algorithm.

3.2. Grid resolution

Simulations across various mesh densities were conducted to assess the influence of mesh resolution on the accuracy of the computational results. Case C1 was analyzed using multiple grid resolutions, governed by the parameter N_m. A free quadrilateral mesh was employed to discretize the computational domain. Details regarding the N_m values and corresponding mesh characteristics are provided in Table 3.

Fig. 5 illustrates the numerical prediction of MVF during the solid–liquid phase change for different mesh resolutions. The near-complete overlap of the curves demonstrates the high degree of precision obtained in the simulations. Fig. 6 provides a detailed view of the selected mesh ($N_m = 6$), highlighting the refined structure near critical regions such as the tube walls and metal foam interfaces, which ensures precise resolution of thermal gradients and phase boundaries.

In this study, a detailed timestep analysis was not required as the chosen time step and the adaptive time-stepping method used in the simulations were sufficient to ensure both stability and accuracy. The adaptive time-stepping method, controlled by the BDF scheme, automatically adjusts the time step to maintain the relative error below, providing accurate results throughout the simulations. Therefore, further timestep analysis was not necessary. This approach has been validated through grid independence testing and ensures that the results are both reliable and computationally efficient. It is noteworthy that the temporal step size was adaptively controlled using the BDF scheme to ensure a relative tolerance below 1×10^{-4}. The analysis indicated that employing a finer mesh with $N_m = 3$ considerably reduced the required time step size, thereby enhancing the solution accuracy. However, this refinement also increased the total computational cost. As a result, a mesh with $N_m = 3$ was chosen as the optimal configuration, providing a suitable balance between computational accuracy and efficiency.

The N_m parameter is the mesh control parameter, which dictates the resolution of the computational grid. Increasing N_m results in a finer grid with more mesh elements, thereby enhancing the accuracy of the simulation but increasing computational cost. In the context of this study, N_m was varied to assess the sensitivity of the results to grid resolution.

3.3. Model and code validation

The validity and reliability of the present computational model and simulation results were assessed by comparison with the experimental findings of Kamkari et al. [9] and the analytical predictions of Kamkari and Amlashi [37]. These reference investigations examined the phase-change behavior of lauric acid as a PCM within a rectangular cavity measuring 120 × 50 mm, where the left boundary wall was maintained at a constant temperature of $T_h = 70$ °C, and all other boundaries were thermally insulated. In the Kamkari et al. [9] modelling a local thermal equilibrium approach was adopted.

A comparison of the MVF between the present simulation and the referenced works is illustrated in Fig. 7. The observed agreement between the outcomes verifies the precision and reliability of the current numerical approach and validates the developed model.

To assess the performance of the present computational framework in simulating the phase-change behavior of paraffin wax composites

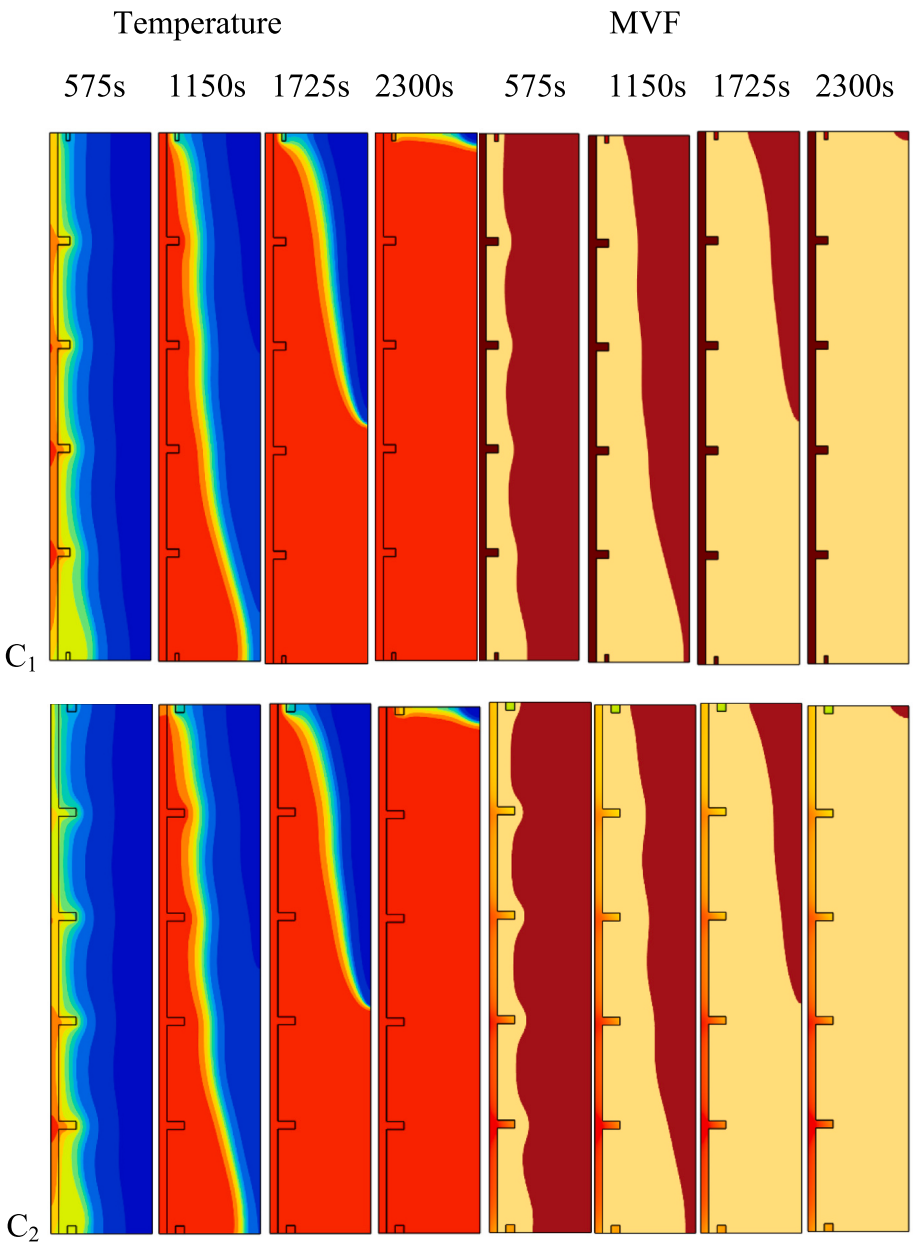

Fig. 13. Isotherms and MVF contours of C1-C11 based on the Table 2 at P_{in} = 3000 Pa and Q_0 = 500 W.

embedded in metallic foam, the numerical results were compared with the experimental observations of Zheng et al. [28]. In the referenced study, the phase transition of paraffin wax was conducted inside a cubic cavity with dimensions of 100 mm per side, where one vertical wall was maintained under a constant heat flux of 1150 W. Minor thermal losses were reported from the lateral boundaries of the system. The metallic foam used in the experiment had a porosity of 0.95 and a pore density of 5 PPI.

Fig. 8 presents the evolution of the melting front at heating durations of 1.5, 3, and 4.5 h. Fig. 9 shows a comparison of the average wall temperatures. The simulated phase interface shape and position closely align with the experimental observations reported in [28]. The temperature profiles also show a good match between the simulations and the experimental observations.

4. Results and discussion

4.1. Effect of fin size on melting process

Fig. 10 depicts the variations of the MVF and the outlet velocity of the PCM V_{out} as functions of time for the different configurations considered, C_1 to C_{11}. In all the cases, the MVF starts increasing slowly from zero where the PCM is in the solid state, then the rise of MVF becomes sharper as more PCM melts due to the enhanced convective heat transfer in the enclosure. It is clear that the melting rate of the PCM is maximum in case C_1 (fin size is 20 % of the total width) and minimum in case C_{11} (fin size is 70 % of the total width). The total melting duration is 27 % longer in the latter compared to the former. In the intermediate cases, the melting rate increases progressively by going from a case to the following one. This is due to the fact that the cases are classified by the scale of the fin, and increasing the fin size creates an obstruction to the flow of the melted PCM, hindering further PCM melting in the cavity.

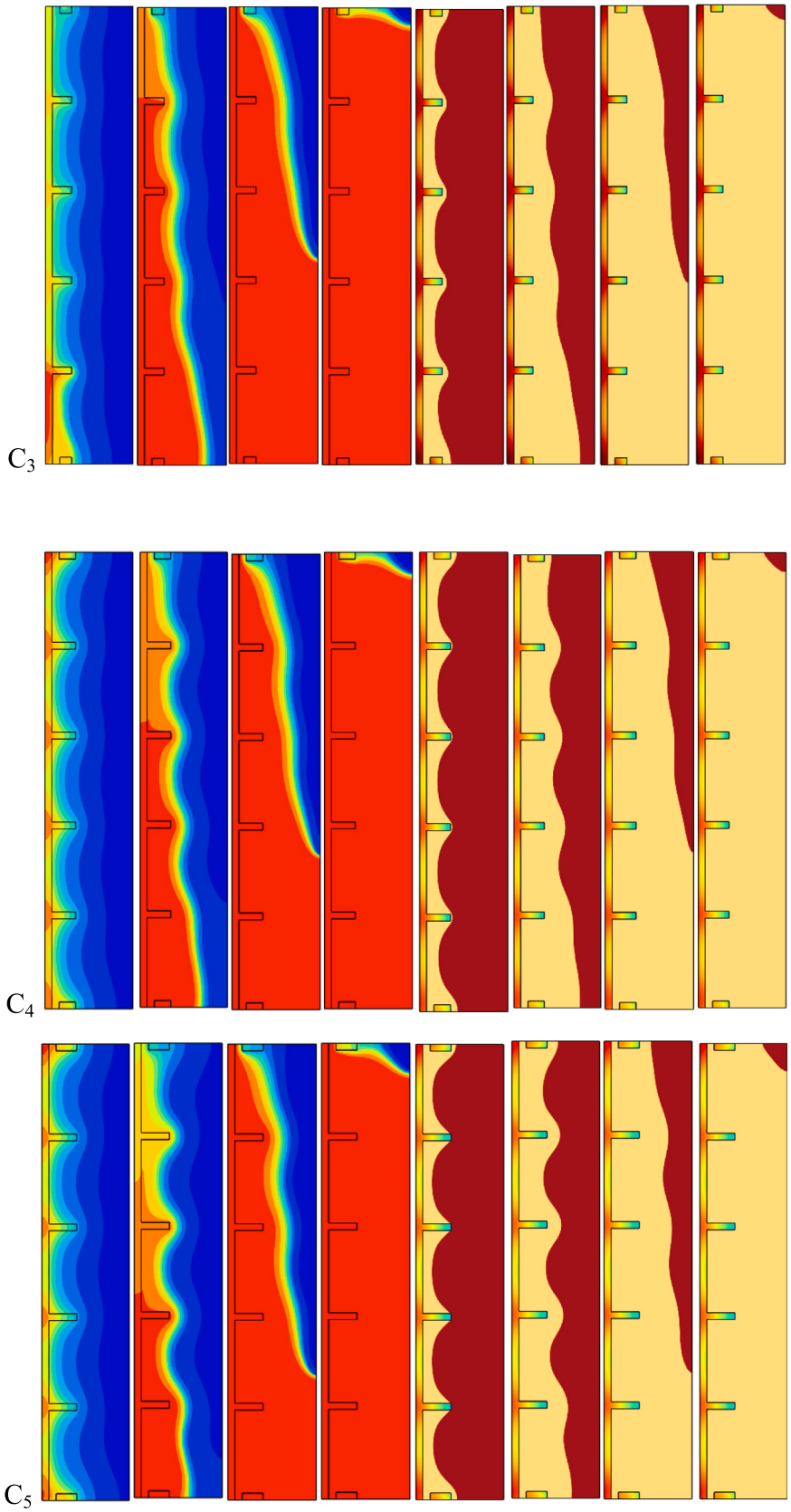

Fig. 13. (*continued*).

These results show that, in the present dynamic-melting configuration with metal foam, increasing fin length beyond 0.2 L slows down the global melting process, because the enlarged fin surfaces progressively obstruct the convective circulation of the liquid PCM. Fins still promote local conduction in the vicinity of the nichrome wall and accelerate the initial formation of a liquid layer; however, once a continuous liquid

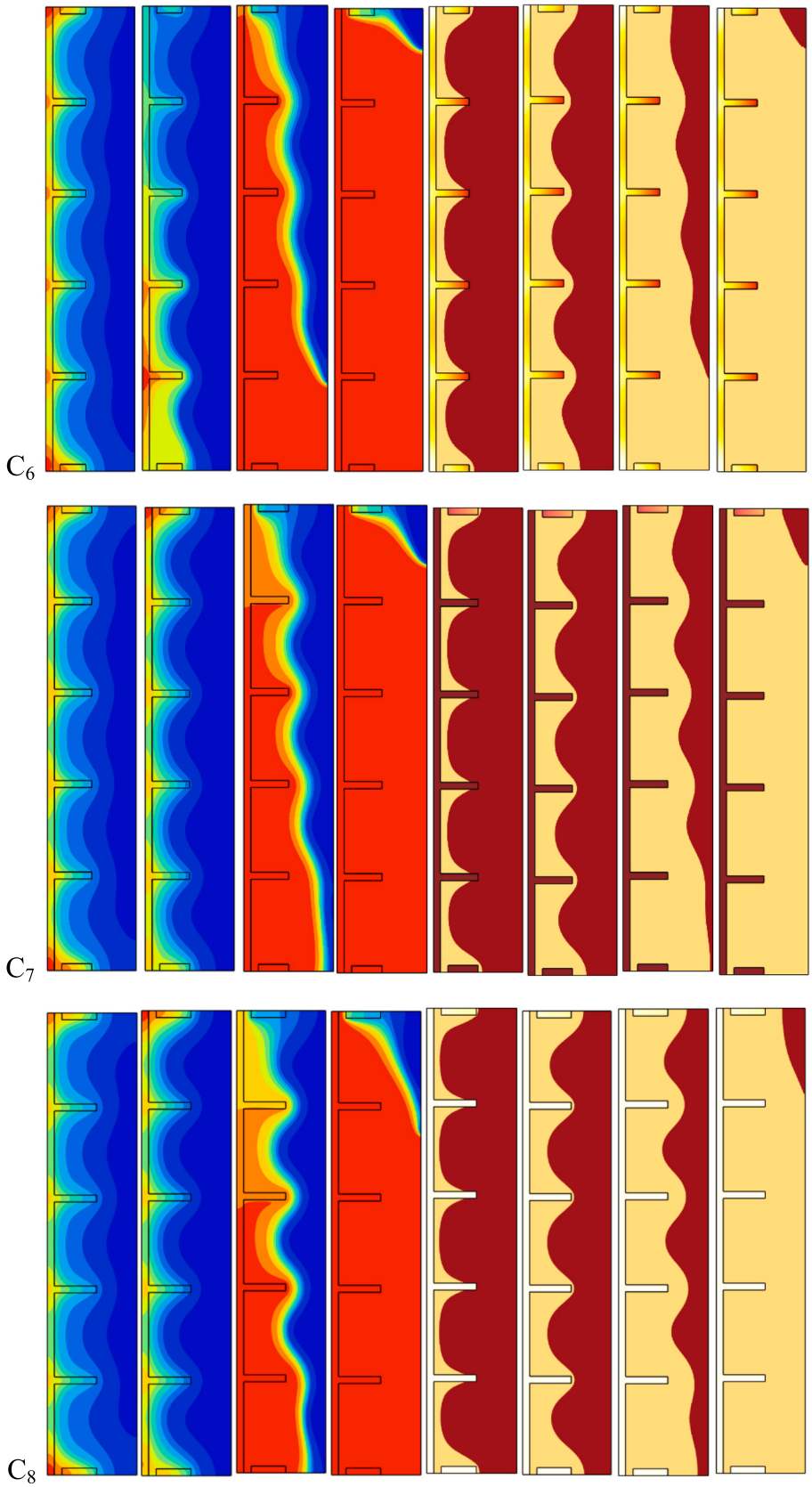

Fig. 13. (*continued*).

path is established, global heat transfer is dominated by buoyancy-driven and forced convection. In this regime, overly long fins behave mainly as flow barriers rather than as beneficial conduction extensions.

As for V_{out}, it also starts from zero due to the absence of flow in the solid PCM, then gradually increases as the melted PCM moves between the inlet and the outlet. The onset of liquid motion occurs earliest in case C1,

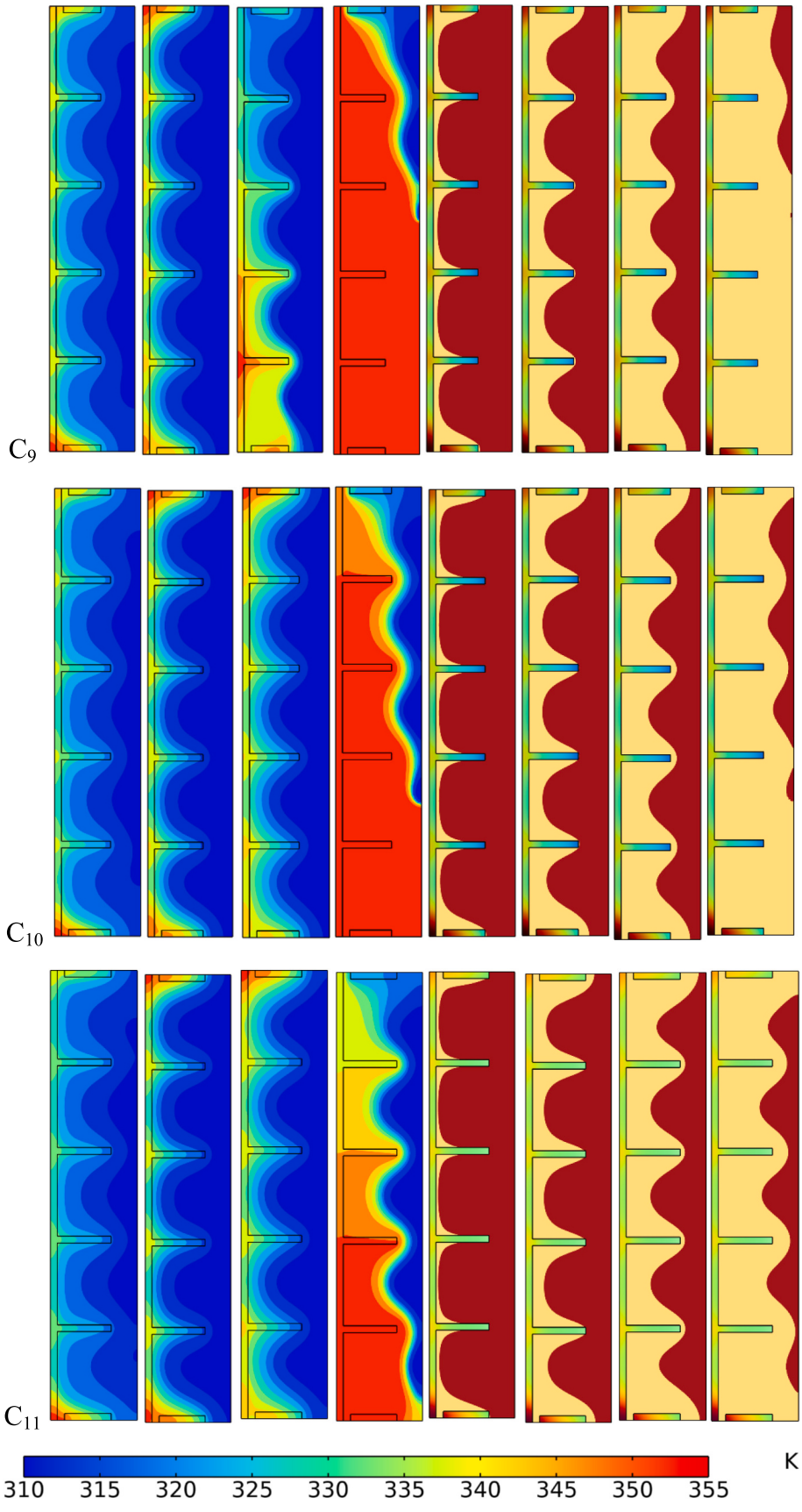

Fig. 13. (*continued*).

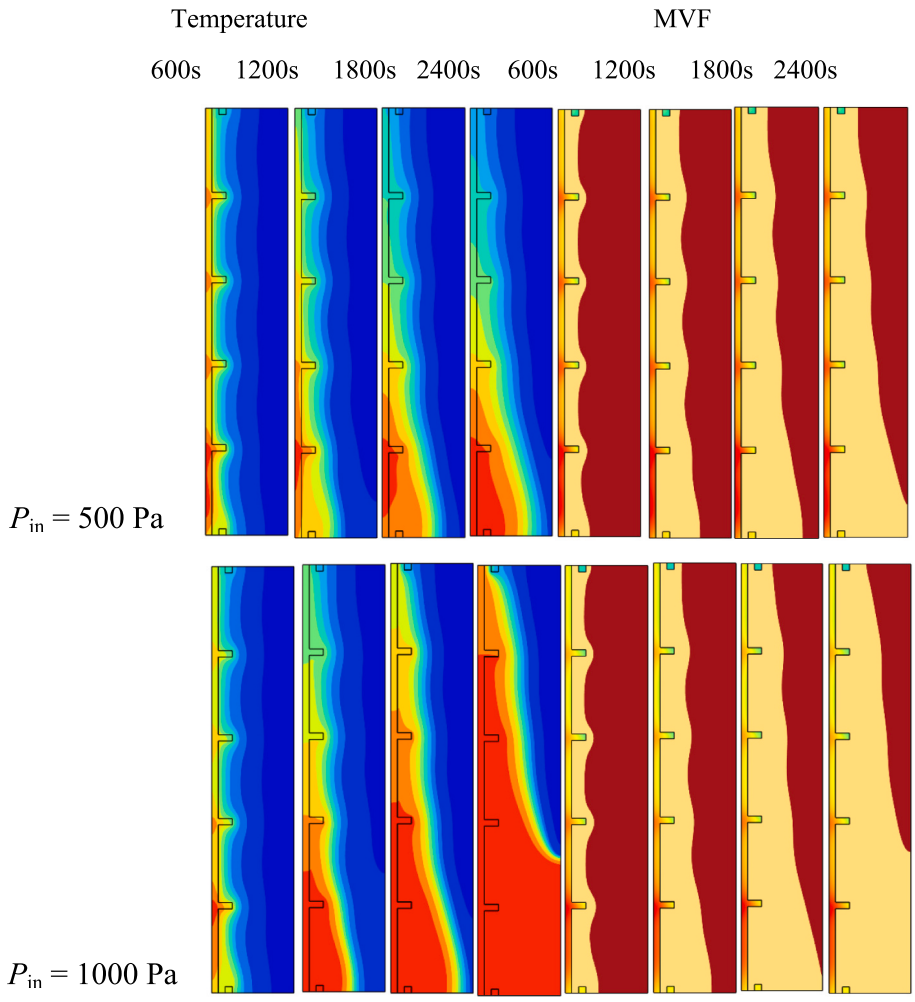

Fig. 14. Isotherms and MVF contours across different pressures at w = 0.25 L (C2) and Q_0 = 500 W (C18-C22).

starting after 2100 s, and latest in case C11, starting after 2800 s. In addition, the outlet speed at every instant rises inversely with the scale of the fins. In particular, a 10 % rise in the maximum speed is obtained in case C_1 compared to case C_{11}. These observations confirm the negative effect of the large fins on the liquid PCM circulation within the enclosure.

Although the external flowing cycle effectively accelerates the melting process of PCMs, its cost-effectiveness remains an important consideration. The energy required to drive the external flow should be evaluated against the enhanced performance achieved in melting the PCM. Future studies should investigate the balance between these two factors to optimize both energy consumption and melting efficiency.

4.2. Impact of inlet pressure on PCM melting

The impact of the various inlet pressures P_{in} on the time variations of MVF and V_{in} is illustrated in Fig. 11 for the case C_2. It's noted that the PCM melting speed increases with P_{in}. The PCM takes around 2 times less time to fully melt for P_{in} = 3000 Pa compared to P_{in} = 500 Pa. Even when P_{in} is only raised from 500 Pa to 1000 Pa, a 51 % in the melting rate is obtained. This is due to the fact that a higher inlet pressure of the PCM results in intensified flow and enhanced heat transfer at the melting interface, leading to faster melting. In addition, and for the same reason, it can be seen that the maximum V_{out} is higher in the case of P_{in} = 1000 Pa compared to P_{in} = 500 Pa. This increase becomes 2.6 times if the inlet pressure is further increased from 500 Pa to 3000 Pa. While the increase in inlet pressure is shown to enhance forced convection in a linear fashion, it is important to note that further studies should explore potential non-linear effects and examine the long-term impact of pressure variations at higher flow rates and different configurations.

4.3. Effect of heating rate on melting performance

The variations of MVF and V_{out} as functions of time for the different heating rates Q_0 are plotted in Fig. 12. It is evident that decreasing Q_0 can significantly reduce the melting speed. In fact, doubling Q_0 from 250 to 500 W, accelerates the melting process by 189 %. Up to 366 % increase in the melting rate can be achieved by further raising Q_0 from 250 W to 1500 W. Moreover, V_{out} also gets higher when Q_0 is increased since the formation of the liquid film between inlet and outlet ports is faster. These findings are related to the rise in melted PCM when the heat generation source is intensified. Moreover, it is noted that there is no change in the maximum V_{out} can be obtained when Q_0 is reduced from 1500 W to 250 W. This is since the maximum V_{out} is controlled by metal foam and fin structure when the enclosure state is fully liquid PCM. The hydrodynamic behavior of the system is independent of Q_0. However, the onset of liquid PCM flows appears earlier in the former case compared to the latter. Namely, PCM starts flowing through the outlet after 5900 s for Q_0 = 250 W, but only after 1500 s for Q_0 = 1500 W. Naturally, increasing the intensity of the heating source accelerates melting. Still, once all the PCM has melted, a similar flow pattern appears, as the inlet pressure and fin size are the same, so the speed of the

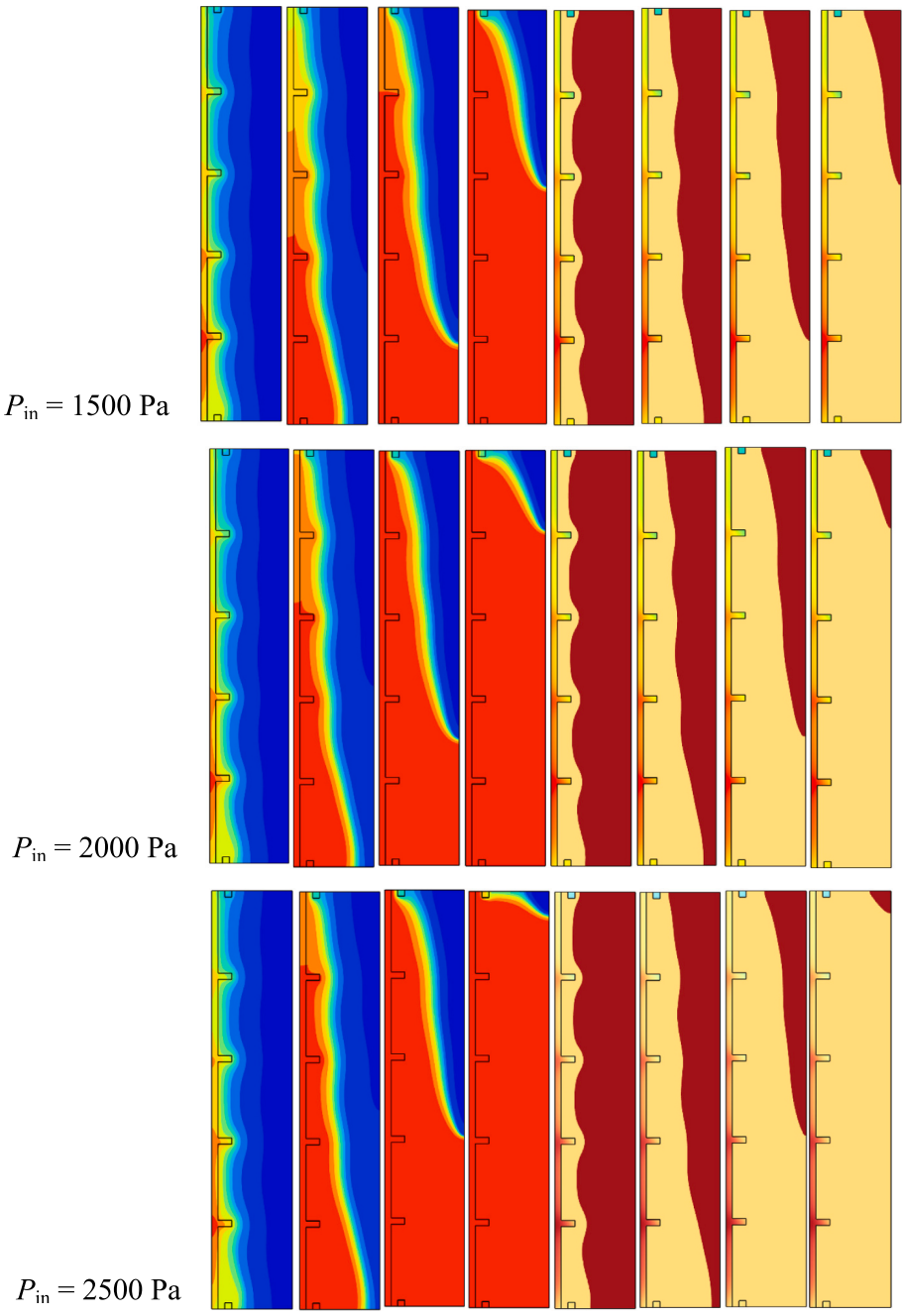

Fig. 14. (*continued*).

flow is not affected. In addition to the effect of inlet pressure on melting, it is essential to note the influence of PCM flow dynamics, where the bottom part of the system tends to be hotter than the upper part. This temperature gradient enhances the flow of liquid PCM from the heated regions to the cooler areas, contributing to improved heat transfer and accelerating the melting process.

4.4. Analysis of thermal and melting contours

The evolution of the isotherms and MVF contours is shown in Fig. 13 for the different configurations C_1 to C_{11}. In all the cases, a film of melted PCM initially appears near the finned hot wall, then as time goes by, further melting occurs until finally almost all the PCM in the cavity has melted. The last solid PCM to melt is located in the top right corner of the enclosure. This is because the heat transfer in the open space of the cavity is primarily driven by convection. As the hot liquid PCM near the left wall rises, it melts the solid PCM, cools, and moves downward, repeating the cycle. This process is illustrated in Fig. 13, which shows the progression of melting across different times. It can be seen also that PCM melts initially in the zone neighboring the fins, in that zone, heat transfer is dominated by conduction as indicated by the stratified isotherms. Because of the fins' high thermal conductivity, heat transfer to the nearby PCM is enhanced, leading to melting in that region. The melting front of the PCM exhibits protrusions of liquid PCM near the fin boundaries, while larger solid PCM protrusions appear in the spaces separating the fins. It should be emphasized that as the fin size increases, the overall melting rate of the PCM becomes slower. By comparing the cases C_1 to C_{11}, their main feature is the scale of the fins, which varies from 20 % to 70 % of the cavity width. It is seen that melting slows down progressively by moving from the smallest fin scale (C_1) to the largest

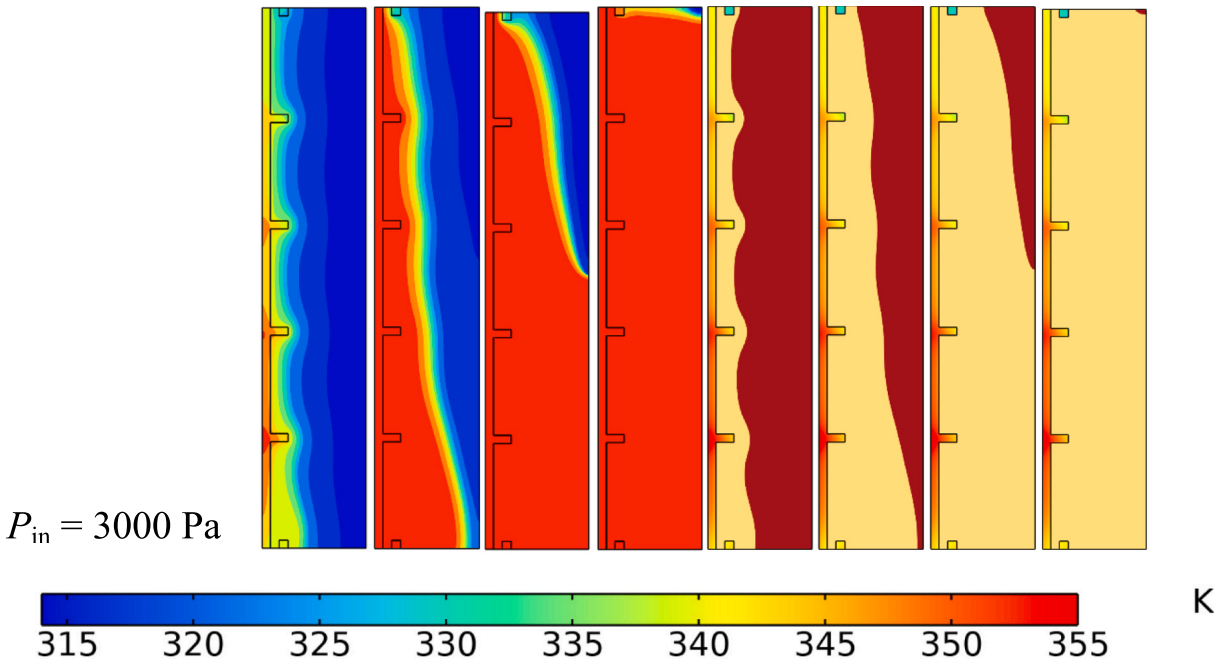

Fig. 14. (*continued*).

(C_{11}). Indeed, the presence of the fins provides an improvement of the effective thermal conductivity, but its impact on PCM melting remains localized near the fins as previously mentioned. Once a melted PCM film appears near the finned wall, the melting behavior becomes dominated by convection. In this case, the presence of the fins represents a barrier slowing down the liquid circulation and inhibiting PCM melting over the whole enclosure.

The influence of P_{in} on the thermal and melting contours is illustrated in Fig. 14 for the configuration C_2. At the beginning, the PCM shows the same behavior in all the cases. But soon after, the impact of P_{in} appears to enhance heat transfer and accelerate melting. It is seen that the amount of melted PCM is very low for P_{in} = 500 Pa compared to when P_{in} = 3000 Pa. In the former, most of the PCM remains in the solid state even after 2400 s, while in the latter, almost all the PCM has melted after that duration. For the intermediate values of P_{in}, it is seen that PCM is more pronounced as P_{in} is increased. In fact, P_{in} is related to the flow of hot PCM entering the cavity. Raising P_{in} further opens the passage between the inlet and the outlet. This pressurized stream of hot liquid PCM intensifies the convective heat transfer across the PCM, resulting in enhanced melting. On the other hand, considerably reducing P_{in} shifts the configuration towards an enclosure with little to no PCM circulation between the inlet and the outlet, such that the effect of pressurizing the PCM at the inlet becomes negligible. The inlet is at the bottom, so the fresh hot PCM first reaches the lower region and melts the bottom section more effectively than the top section.

The isothermal and melting contours are depicted in Fig. 15 for various heating rates Q_0. Similar to the impact of P_{in}, increasing Q_0 also helps in accelerating PCM melting. For Q_0 = 250 W, almost all the PCM in the enclosure remains in the solid phase after 1500 s, while most of the PCM changes into the liquid phase within 1125 s if Q_0 is raised to 1500 W. The other cases, where Q_0 is varied in the interval between 250 W and 1500 W, show a progressive enhancement in PCM melting with the rise of Q_0. Indeed, the source of heating in the enclosure is the internal heat generation in the wall represented by Q_0. When the heating source is strengthened, and for a constant pressure inlet and a given fin scale, the heat absorbed by the PCM increases, contributing to intensified PCM melting.

5. Conclusions

The present study was dedicated to the thermal and flow behaviors of PCM in an LHTES unit. The unit is cylindrical and is filled with PCM in its annulus. The system also integrates metal foam within the PCM domain to enhance heat transfer. An external flowing cycle is dedicated to circulating pressurized hot PCM inside the enclosure. A heating element is located at the cavity wall such that the value of the heat rate provided can be varied. Fins with variable scale are located on the left wall. Their scale can vary between 20 % and 70 % of the cavity width. The influence of various parameters, such as the fin scale, the inlet pressure P_{in} of the pressurized PCM, and the heat rate in the wall, on the thermal and melting contours, as well as on the melted volume fraction and outlet velocity of the PCM (V_{out}) was assessed. The main findings are the following:

- Raising the size of the fins reduces the melting speed, as larger fins create an obstacle hindering the circulation of the melted PCM and diminishing the convective heat transfer. Melting was found to be 27 % slower when the fin size was 70 % of the cavity width compared to when it was 20 %. In addition, 10 % increase in the outlet speed of the melted PCM was observed in the latter case compared to the former.
- A higher value of P_{in} led to more intense PCM melting, due to the accelerated liquid circulation. Namely, a 51 % and 200 % rise in the melting rate was obtained when P_{in} was raised from 500 Pa to 1000 Pa and 3000 Pa, respectively. In addition, 0.5 and 2.6 times increase in V_{out} was observed when P_{in} was augmented from 500 Pa to 1000 Pa and 3000 Pa, respectively.
- PCM melting rate can be enhanced by raising the value of Q_0. The melting duration was reduced by 189 % and 366 % when Q_0 was raised from 250 W to 500 W and 1500 W, respectively. Nonetheless, even if increasing Q_0 leads to a faster cooling, the flow of the PCM has the same value of V_{out} once all the PCM has melted, given the same value of P_{in} and the same scale of the fins.

The presence of metal foam within the PCM domain significantly enhances heat transfer, facilitating faster PCM melting and improving the overall performance of the LHTES system. The external flowing

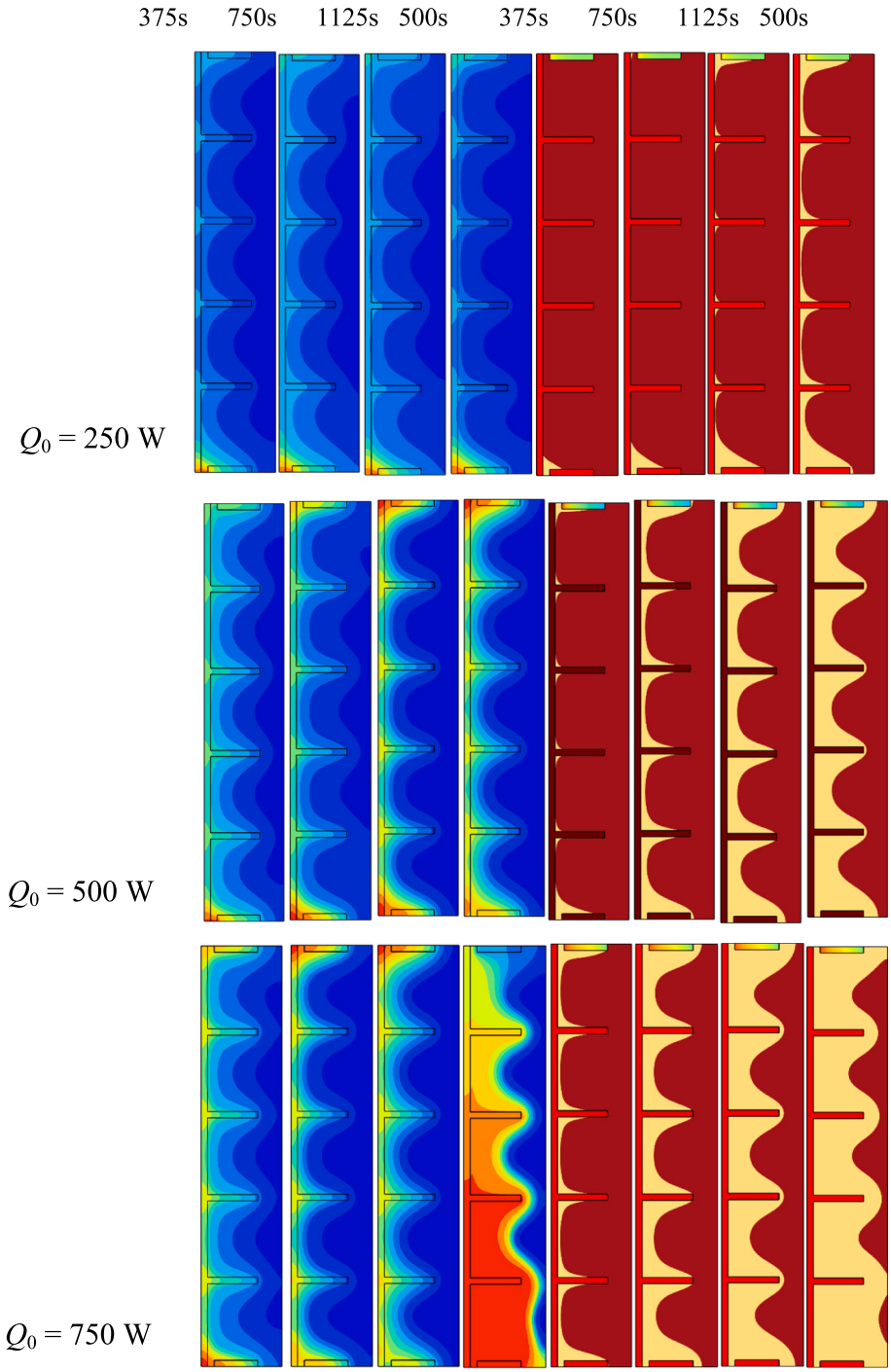

Fig. 15. Isotherms and MVF contours for different Q_0 at w = 0.7 L (C11), P_{in} = 3000 Pa and V_{out} = 0.207276 m/s (cases 17 to 22).

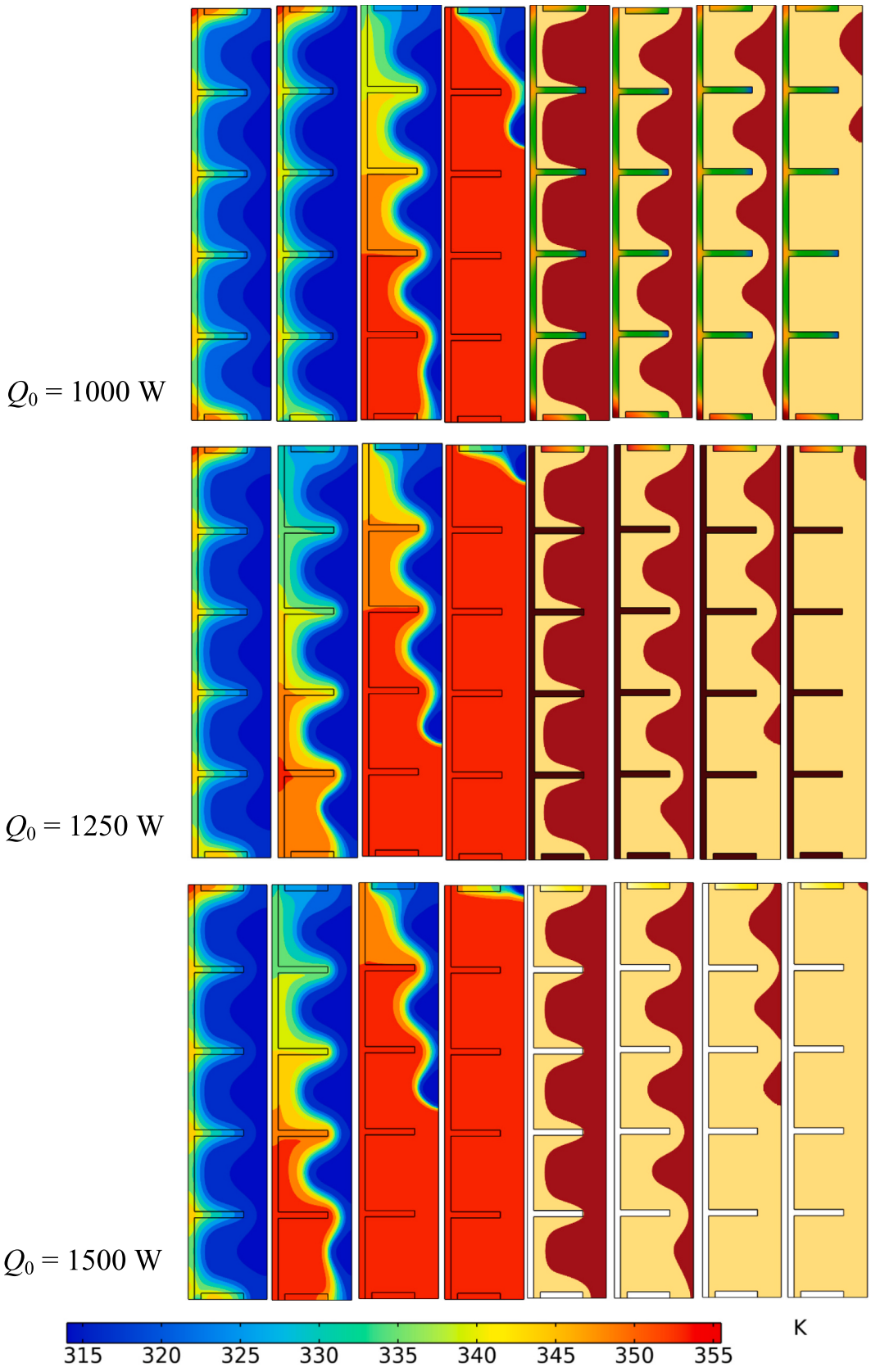

Fig. 15. (*continued*).

cycle, therefore, appears to be a promising means to enhance the melting performance of LHTES units at relatively low driving pressures. Nonetheless, a comprehensive assessment of cost-effectiveness, including auxiliary pumping power, capital, and maintenance costs of the external circuit, was not addressed in this work. Coupling the present model with a hydraulic and techno-economic analysis is recommended as a key

topic for future research.

CRediT authorship contribution statement

Mohamed Bouzidi: Writing – review & editing, Writing – original draft, Investigation, Formal analysis, Conceptualization. **Zehba Raizah:** Writing – review & editing, Writing – original draft, Visualization, Methodology, Investigation, Conceptualization. **Bhupendra Singh Chauhan:** Writing – review & editing, Writing – original draft, Methodology, Conceptualization. **Ahmad Hajjar:** Writing – review & editing, Writing – original draft, Resources, Methodology, Funding acquisition, Formal analysis, Data curation. **T. Anwor:** Writing – review & editing, Writing – original draft, Validation, Methodology, Investigation, Conceptualization. **Mansour Mohamed:** Writing – review & editing, Writing – original draft, Methodology, Investigation, Conceptualization. **Hammadi Khmissi:** Writing – review & editing, Writing – original draft, Methodology, Investigation, Formal analysis, Data curation. **Mehdi Ghalambaz:** Writing – review & editing, Writing – original draft, Validation, Supervision, Project administration, Conceptualization.

Declaration of competing interest

The authors declare that they have no known competing financial interests or personal relationships that could have appeared to influence the work reported in this paper.

Acknowledgments

The authors extend their appreciation to the Deanship of Research and Graduate Studies at King Khalid University for funding this work through large Research Group Project under the grant number (RGP2/395/46). The authors extend their appreciation to the Deanship of Scientific Research at Northern Border University, Arar, KSA for funding this research work through the project number “NBU-FPEJ-2026-2222-01”.

Data availability

Data will be made available on request.

References

[1] H. Togun, H.S. Sultan, H.I. Mohammed, A.M. Sadeq, N. Biswas, H.A. Hasan, R. Z. Homod, A.H. Abdulkadhim, Z.M. Yaseen, P. Talebizadehsardari, A critical review on phase change materials (PCM) based heat exchanger: different hybrid techniques for the enhancement, J. Energy Storage 79 (2024) 109840.
[2] F.L. Rashid, H.I. Mohammed, A. Dulaimi, M.A. Al-Obaidi, P. Talebizadehsardari, S. Ahmad, A. Ameen, Analysis of heat transfer in various cavity geometries with and without nano-enhanced phase change material: a review, Energy Rep. 10 (2023) 3757–3779.
[3] R. Kalbasi, A. Sedaghat, K. Khanafer, A. Al-Masri, An experimental study on application of phase change materials in a portable cabin in wintertime of Kuwait under active/passive cooling, Appl. Therm. Eng. 257 (2024) 124429.
[4] H.M. Ali, T.-U. Rehman, M. Arıcı, Z. Said, B. Duraković, H.I. Mohammed, R. Kumar, M.K. Rathod, O. Buyukdagli, M. Teggar, Advances in thermal energy storage: fundamentals and applications, Prog. Energy Combust. Sci. 100 (2024) 101109.
[5] Z. Han, Q. Liu, M. Cong, W. Ge, S. Ding, Optimization of the annular fin arrangement in phase change heat storage units based on response surface methodology, Appl. Therm. Eng. 257 (2024) 124479.
[6] T.T.M. Rocha, M. Teggar, J. Khan, P.V. Trevizoli, R.N. de Oliveira, J. Khodadadi, Comprehensive effective thermal conductivity correlation and fast model for the melting of a phase change material inside a horizontal shell-and-tube unit, Appl. Therm. Eng. 257 (2024) 124497.
[7] F.L. Rashid, A. Rahbari, R.K. Ibrahem, P. Talebizadehsardari, A. Basem, A. Kaood, H.I. Mohammed, M.H. Abbas, M.A. Al-Obaidi, Review of solidification and melting performance of phase change materials in the presence of magnetic field, rotation, tilt angle, and vibration, J. Energy Storage 67 (2023) 107501.
[8] S. Jegadheeswaran, A. Sundaramahalingam, S.D. Pohekar, Alternative heat transfer enhancement techniques for latent heat thermal energy storage system: a review, Int. J. Thermophys. 42 (2021) 1–48.
[9] B. Kamkari, H. Shokouhmand, F. Bruno, Experimental investigation of the effect of inclination angle on convection-driven melting of phase change material in a rectangular enclosure, Int. J. Heat Mass Transf. 72 (2014) 186–200.
[10] A. Egea, A. García, R. Herrero-Martín, J. Pérez-García, Experimental performance of a novel scraped surface heat exchanger for latent energy storage for domestic hot water generation, Renew. Energy 193 (2022) 870–878.
[11] M. Boujelbene, S.A. Mehryan, M. Sheremet, M. Shahabadi, N.B. Elbashir, M. Ghalambaz, Numerical Study of a Non-Newtonian Phase Change Flow in Finned Rectangular Enclosures, Facta Universitatis, Mechanical Engineering, Series, 2024.
[12] A. Sangtarash, S.R. Maadi, R.A. Taylor, A. Arabkoohsar, S. Wongwises, M. Sheremet, O. Mahian, A.Z. Sahin, A comprehensive investigation of porous media's effects on the performance of photovoltaic thermal systems, Appl. Therm. Eng. 245 (2024) 122766.
[13] S. Hansda, A. Chattopadhyay, S.K. Pandit, M.A. Sheremet, Thermosolutal performance of a non-Newtonian Casson fluid in a curvilinear porous baffled chamber with irreversibility and various heating strategies, Phys. Fluids 37 (2025).
[14] S. Sabet, B. Buonomo, M.A. Sheremet, O. Manca, Numerical investigation of melting process for phase change material (PCM) embedded in metal foam structures with kelvin cells at pore scale level, Int. J. Heat Mass Transf. 214 (2023) 124440.
[15] V.R. Voller, C. Prakash, A fixed grid numerical modelling methodology for convection-diffusion mushy region phase-change problems, Int. J. Heat Mass Transf. 30 (1987) 1709–1719.
[16] S. Zhang, Y. Yao, Y. Jin, Z. Shang, Y. Yan, Heat transfer characteristics of ceramic foam/molten salt composite phase change material (CPCM) for medium-temperature thermal energy storage, Int. J. Heat Mass Transf. 196 (2022) 123262.
[17] D.A. Nield, A. Bejan, Convection in Porous Media, Springer, 2006.
[18] F. Alimi, H.S.S. Aljibori, M. Bouzidi, A. Alasmari, S. Yazdani, M. Ghalambaz, Improving a shell-tube latent heat thermal energy storage unit for building hot water demand using metal foam inserts at a constant pumping power, J. Build. Eng. 98 (2024) 111040.
[19] J. Shafi, M. Ghalambaz, M. Fteiti, M. Ismael, M. Ghalambaz, Computational modeling of latent heat thermal energy storage in a shell-tube unit: using neural networks and anisotropic metal foam, Mathematics 10 (2022) 4774.
[20] Y. Yao, H. Wu, Interfacial heat transfer in metal foam porous media (MFPM) under steady thermal conduction condition and extension of Lemlich foam conductivity theory, Int. J. Heat Mass Transf. 169 (2021) 120974.
[21] C. Zhao, J. Wang, Y. Sun, S. He, K. Hooman, Fin design optimization to enhance PCM melting rate inside a rectangular enclosure, Appl. Energy 321 (2022) 119368.
[22] N. Modi, X. Wang, V. Kumar, D. Milani, M. Negnevitsky, K.C. Ng, Impact of key parameters on the numerical modelling of phase-changing phenomena in horizontal latent heat thermal energy storage, Appl. Therm. Eng. 257 (2024) 124419.
[23] Y. Yao, H. Wu, Macroscale modeling of solid–liquid phase change in metal foam/paraffin composite: effects of paraffin density treatment, thermal dispersion, and interstitial heat transfer, J. Therm. Sci. Eng. Appl. 13 (2021).
[24] Y. Yao, H. Wu, Z. Liu, Direct simulation of interstitial heat transfer coefficient between paraffin and high porosity open-cell metal foam, J. Heat Transf. 140 (2018).
[25] A.I.N. Korti, H. Guellil, Experimental study of the effect of inclination angle on the paraffin melting process in a square cavity, J. Energy Storage 32 (2020) 101726.
[26] A. Agarwal, R. Sarviya, Characterization of commercial grade paraffin wax as latent heat storage material for solar dryers, Mater. Today Proc. 4 (2017) 779–789.
[27] N. Ukrainczyk, S. Kurajica, J. Šipušić, Thermophysical comparison of five commercial paraffin waxes as latent heat storage materials, Chem. Biochem. Eng. Q. 24 (2010) 129–137.
[28] H. Zheng, C. Wang, Q. Liu, Z. Tian, X. Fan, Thermal performance of copper foam/paraffin composite phase change material, Energy Convers. Manag. 157 (2018) 372–381.
[29] S.-K. Choi, S.-O. Kim, T.-H. Lee, Dohee-Hahn, computation of the natural convection of nanofluid in a square cavity with homogeneous and nonhomogeneous models, Numer. Heat Transf. A Appl. 65 (2014) 287–301.
[30] O.C. Zienkiewicz, R.L. Taylor, P. Nithiarasu, The Finite Element Method for Fluid Dynamics, Seventh Edition ed, Butterworth-Heinemann, Oxford, 2014.
[31] D. Pepper, The Intermediate Finite Element Method: Fluid Flow and Heat Transfer Applications, Routledge, 2017.
[32] C.T. Kelley, Solving Nonlinear Equations with Newton's Method, SIAM, 2003.
[33] P. Deuflhard, Newton Methods for Nonlinear Problems: Affine Invariance and Adaptive Algorithms, Springer Science & Business Media, 2005.
[34] M. Bollhöfer, O. Schenk, R. Janalik, S. Hamm, K. Gullapalli, State-of-the-art sparse direct solvers, in: Parallel +Algorithms in Computational Science and Engineering, 2020, pp. 3–33.
[35] M. Bollhöfer, A. Eftekhari, S. Scheidegger, O. Schenk, Large-scale sparse inverse covariance matrix estimation, SIAM J. Sci. Comput. 41 (2019) A380–A401.
[36] G. Söderlind, L. Wang, Adaptive time-stepping and computational stability, J. Comput. Appl. Math. 185 (2006) 225–243.
[37] B. Kamkari, H.J. Amlashi, Numerical simulation and experimental verification of constrained melting of phase change material in inclined rectangular enclosures, Int. Commun. Heat Mass Transf. 88 (2017) 211–219.